Check for updates

ADVANCING EARTH AND SPACE SCIENCE

JGR Solid Earth

RESEARCH ARTICLE
10.1029/2021JB022964

Key Points:

- Transient dimensionless solutions of length, spacing, aperture, and pattern of *multiple* thermal fractures were obtained and validated
- Scaling laws of late-time fracture length (linear with square root of cooling time) were obtained for single and multiple thermal fractures
- The solutions and scaling laws provide time profiles as a function of thermal stress ratio that covers all reservoir and cooling conditions

Correspondence to:
Q. Zhou,
qzhou@lbl.gov

Citation:
Chen, B., & Zhou, Q. (2022). Scaling behavior of thermally driven fractures in deep low-permeability formations: A plane strain model with 1-D heat conduction. *Journal of Geophysical Research: Solid Earth*, *127*, e2021JB022964. https://doi.org/10.1029/2021JB022964

Received 5 AUG 2021
Accepted 21 JAN 2022

Author Contributions:
Conceptualization: Quanlin Zhou
Data curation: Bin Chen
Formal analysis: Bin Chen, Quanlin Zhou
Funding acquisition: Quanlin Zhou
Investigation: Quanlin Zhou
Methodology: Bin Chen
Project Administration: Quanlin Zhou
Resources: Quanlin Zhou
Software: Bin Chen
Supervision: Quanlin Zhou
Validation: Bin Chen, Quanlin Zhou
Visualization: Bin Chen
Writing – original draft: Bin Chen
Writing – review & editing: Quanlin Zhou

© 2022 Lawrence Berkeley National Laboratory.
This is an open access article under the terms of the Creative Commons Attribution-NonCommercial-NoDerivs License, which permits use and distribution in any medium, provided the original work is properly cited, the use is non-commercial and no modifications or adaptations are made.

Scaling Behavior of Thermally Driven Fractures in Deep Low-Permeability Formations: A Plane Strain Model With 1-D Heat Conduction

Bin Chen[1] **and Quanlin Zhou**[1]

[1]Division of Energy Geosciences, Lawrence Berkeley National Laboratory, Berkeley, CA, USA

Abstract Injection of cold fluids through/into deep formations may cause *significant* cooling, thermal stress, and possible thermal fracturing. In this study, the thermal fracturing of low-permeability formations under one-dimensional heat conduction was investigated using a plane strain model. Dimensionless governing equations, with dimensionless fracture length $\mathcal{L}$, aperture Ω, spacing $\mathcal{D}$, time τ, and effective confining stress $\mathcal{T}$, were derived. Solution of *single* thermal fracture was derived analytically, while solution of *multiple* fractures with constant (or dynamic) spacing were obtained using the displacement discontinuity method (and stability analysis). For single fracture, $\mathcal{L}(\tau, \mathcal{T})$ increases nonlinearly with $\sqrt{\tau}$ and then transitions to scaling law $\mathcal{L} = f(\mathcal{T})\sqrt{\tau}$, indicating that late-time fracture length increases linearly with the square root of cooling time. For *constantly* spaced fractures, $\mathcal{L}(\tau, \mathcal{T}, \mathcal{D})$ deviates from the single-fracture solution at a later τ for a larger $\mathcal{D}$, showing slower propagation under inter-fracture *stress interaction*. For *dynamically* spaced fractures, *fracture arrest* induced by stress interaction was determined by the stability analysis; the fully transient solution provides evolution of dimensionless fracture length, spacing, aperture, and pattern; a similar scaling law, $\mathcal{L} = f'(\mathcal{T})\sqrt{\tau}$ with $f'(\mathcal{T}) < f(\mathcal{T})$, obtained shows the effect of both stress interaction and fracture arrest. The solution and scaling law provide fast predictions for all reservoir and cooling conditions using (single) model parameter $\mathcal{T}$. Application to a geothermal site with $\mathcal{T} = 0.11$ demonstrates that thermal fractures reach 0.67, 6.25, and 78.00 m in length, 0.49, 2.30, and 13.00 m in spacing, and 0.43, 2.09, and 12.19 mm in aperture at 1, 100, and 10,000 days.

Plain Language Summary Thermal fracturing of relatively hot rock in the subsurface can be caused by fluid circulation/flow through hydraulic/natural fractures. Under significant cooling-induced thermal stresses, parallel transverse thermal fractures initiate at the surface of a hydraulic/natural fracture. During their propagation, some fractures are arrested due to fracture interaction, leading to a hierarchically ordered pattern of fractures with increasing spacing. In this study, we investigated these processes using a plane strain model and solved for fracture length, spacing, and aperture in a dimensionless framework. These solutions depend only on one model parameter, dimensionless effective confining stress, in the range of (0, 1) that represents all rock properties, cooling conditions, fluid pressure, and in situ confining stress. The scaling law obtained through fitting the solutions shows that late-time fracture length increases linearly with the square root of cooling time. Application to a geothermal site shows that thermal fractures can slowly propagate to ~80 m, with ~10 m spacing and ~10 mm surface aperture, after 27 years of cold-water circulation under a dimensionless effective confining stress of 0.11. The solution and scaling law can be used to efficiently predict short-term and long-term thermal fracture propagation with arrest.

1. Introduction

Temperature perturbations (ΔT) may be induced by injecting fluids through wellbores into deep, relatively hot reservoirs or by flowing cold fluids through natural or hydraulic fractures and natural faults (Zhou, Oldenburg, Spangler, et al., 2017; Zhou et al., 2019). Reservoir cooling may cause significant thermal stresses near the wellbores and along the natural or hydraulic fractures (Martínez-Garzón et al., 2014; Perkins & Gonzalez, 1984; Stephens & Voight, 1982). The thermal stresses either suffice to initiate tensile fractures at the walls of wellbores or fractures or reduce fracturing pressures in the cooled region so that injection-induced pressure increase (ΔP) can facilitate formation breakdown and initiate such fractures (Perkins & Gonzalez, 1985). The initiated fractures propagate away from the walls into the rock matrix as the temperature perturbations transport under heat conduction in the matrix and heat convection along the newly created fractures and in the permeable matrix. The fracture

propagation in return decreases the injection pressure at the wellbores (showing *enhanced injectivity*) and affects the convective-conductive heat transport in the ΔT-affected region. This two-way coupling includes complicated processes: flow of single-phase or multiphase fluids, heat transport, thermoporoelasticity, and fracture propagation, as documented in some classic books (e.g., Cheng, 2016; Jaeger et al., 2007).

The fracturing driven by thermal stresses, in the absence or presence of pressure increase, of interest in this study is referred to hereafter as *thermal fracturing*, and the thermally driven fractures are referred to as *thermal fractures*. When initiated, they are densely spaced at the cooling wall or surface. Some of the initiated fractures continue to propagate with time, while the others are arrested at different times and distances from the cooling surface under strong inter-fracture stress interaction. The fracture propagation and arrest lead to fracture spacing that changes with time and distance (referred to as *dynamic spacing*) and a hierarchical pattern of propagating and arrested fractures (referred to as *dynamically spaced fractures*), which is very different from that of hydraulic fracturing (Chen et al., 2021). The second key difference is the fact that the effective spatial scales of the physical processes (e.g., propagation of thermal fractures and evolution of ΔT and ΔP plumes) are dramatically different during thermal fracturing associated with long-term fluid injection and flow, while the temporal scale of hydraulic fracturing is short. It is the two key differences that lead to great challenges in accurate and efficient modeling of the coupled processes during thermal fracturing and to better understand the phenomena of fluid flow, heat transport, thermoporoelasticity, and thermal fracturing.

1.1. Field Phenomena of Thermal Fracturing in the Subsurface

Thermal fracturing associated with cold fluid injection through vertical or horizontal wells has been reported from many sites of waterflooding, CO_2 storage, unconventional shale gas and oil production, geothermal energy utilization, enhanced geothermal systems (EGS), and so on.

Thermal fracturing in subsurface reservoirs was first reported in the late 1970s and early 1980s from the fields of waterflooding via injection of cold seawater or produced water from oil and gas fields around the world (Detienne et al., 1998; Morales et al., 1986; Svendson et al., 1991; Williams et al., 1987). It was observed that fracturing pressure gradients were lowered by temperature reductions in step-rate injection tests, injectivity was enhanced by long-term injection of cold water, and injected water preferentially migrated through newly fractured perforated/screened intervals of injection wells, a phenomenon of so-called *flow focusing*. Moreover, further propagation of vertical thermal fractures beyond the injection reservoirs was reported to damage the underlying/overlying seals in some rare cases (Martins et al., 1995). These field observations drove the early development of simplified analytical solutions with thermal stresses considered (Koning, 1985; Koning & Niko, 1985; Perkins & Gonzalez, 1984, 1985) and late site-specific modeling based on thermoporoelasticity (van den Hoek et al., 1999).

Similar field observations were recently reported at the sites of cold, liquid or supercritical, CO_2 injection for geological carbon storage (Rangriz Shokri et al., 2019; Zhou et al., 2020). The maximum temperature reduction varied from 30°C at Ordos, China to 60°C at Cranfield, Mississippi, USA. The field observations of enhanced injectivity and flow focusing were attributed to thermal fracturing induced by high thermal stresses. At these reported sites, pressure increase alone could not lead to formation breakdown and fracture initiation and propagation, and fracture propagation was controlled by thermal stresses within the cooled region. Cyclic cooling of as high as 125°C was recorded by distributed temperature sensing during multistage hydraulic fracturing of a horizontal well in a hot unconventional shale reservoir (Raterman et al., 2018, 2019). Such a strong cooling is expected to initiate and propagate thermal fractures from the cased and unperforated well section. These thermal fractures could have an interplay with subsequent hydraulic fractures for a perforated well section.

Thermal stimulation via cold-water injection was used to increase well injectivity or productivity in geothermal fields with natural fractures of sufficient permeability (e.g., Axelsson et al., 2006; Bradford et al., 2016; Kitao et al., 1995; Siratovich et al., 2011). The injectivity/productivity at many geothermal wells reported was enhanced by a factor of up to 40. The enhancement was attributed to the cleaning of debris or mineral deposits from open fractures intercepted by the wellbore during drilling, the re-opening of natural fractures by thermal contraction, and the creation of new fractures from the thermal stress exerted on the reservoir rocks (Axelsson et al., 2006). The stimulation duration ranged from several hours to several weeks. Enhanced injectivity was also observed in a geothermal reservoir at Raft River, Idaho, USA when cold water was continuously injected over the years (Bradford et al., 2015, 2016). The sustainability of fractures observed during and after long-term shut-ins was

attributed to the irreversible rock contraction. Enhanced injectivity and fracture sustainability were reported at water injection wells used to maintain fluid pressure in geothermal reservoirs.

Short-term thermal fracturing to enhance the permeability of EGS formations with insufficient permeability was tested at some sites. The injectivity was increased by a factor of 2 after a 60-hr thermal stimulation at Rittershoffen, France as the near-well permeability was enhanced (Vidal et al., 2016). The decrease of compressional and shear wave velocities was attributed to thermal fracturing at Fenton Hill, New Mexico (Pearson et al., 1983). However, thermal fracturing has not gained much attention at many EGS sites when compared with hydraulic fracturing or shearing (e.g., Brown et al., 2012; Evans, 2005; Evans et al., 2005), even though thermoporoelasticity has been recognized when water injection with hydraulic stimulation causes significant cooling (Loret, 2019).

Unlike the short-term and long-term thermal fracturing associated with well injection reported above, long-term thermal fracturing was proposed in the 1970s to enhance fracture-matrix heat exchange area during water circulation in EGS operation (Barr, 1980; Demuth & Harlow, 1980; Harlow & Pracht, 1972; Murphy, 1978). Their studies focused on the propagation of *secondary*, transverse thermal fractures initiated from *primary* hydraulic fractures stimulated to form a fracture network for heat extraction. The same concept was proposed to enhance unconventional gas/oil production from a hydraulically stimulated field (Enayatpour et al., 2019; Enayatpour & Patzek, 2013). This type of thermal fracturing with fracture propagation and arrest is investigated in this study.

1.2. Experimental Studies on Thermal Fracturing

Thermal fracturing of rock samples has been imaged in laboratory experiments under heating, cooling, or cyclic thermal loading (Browning et al., 2016; Chaki et al., 2008; Fredrich & Wong, 1986; Shen et al., 2021; H. F. Wang et al., 1989; F. Wang et al., 2019; Wang & Konietzky, 2019). Only a few of these studies focused on cooling-induced fracturing. Browning et al. (2016) and Daoud et al. (2020) found that dense thermal fractures were generated around microstructures after single-cycle or multi-cycle heating and cooling with a peak temperature difference up to 1,100ºC, and these fractures were mainly created during cooling as shown by the rate and energy of acoustic emissions recorded. Experiments with liquid nitrogen were conducted on samples of granite, shale, concrete, or sandstone (Cha et al., 2014, 2017, 2018; Wu et al., 2019; S. Zhang et al., 2018), and a few mesoscale fractures were identified in the broken samples. The experiments with sudden cooling (with ΔT of 25°C–500°C) of gradually heated granite samples and subsequent hydraulic fracturing showed a significant decrease of breakdown pressure with the increase of ΔT, as well as different morphology of hydraulic fractures (Li et al., 2021). On the other hand, thermal shock experiments on ceramic (Bahr et al., 1986; Shao et al., 2011) and glass samples (Geyer & Nemat-Nasser, 1982) without confining stress applied showed a hierarchical pattern of thermal fractures caused by fracture propagation and arrest. The different fracture patterns revealed in the above experiments can be attributed to their setups with varying mechanical and cooling boundary conditions, as well as sample sizes and shapes. Of great interest to subsurface engineering applications are those boundary conditions related to wellbore injection and water circulation/flow along hydraulic/natural fractures.

1.3. Modeling of Thermal Fracturing in the Subsurface

Thermal fracturing has been investigated using simplified analytical models. The thermal stresses around a cooled wellbore were computed based on either the solutions of one-dimensional radial cooling (Stephens & Voight, 1982) or the step cooling in a circular or elliptical cooled region using energy balance (Perkins & Gonzalez, 1984, 1985). A highly simplified fracture model was developed by Perkins and Gonzalez (1985) to predict the propagation of thermal fractures in the elliptical cooled region. Koning (1985) and Koning and Niko (1985) developed an analytical model to estimate the geometry of a waterflood-induced fracture driven by both poroelastic and thermoelastic stresses. These early solutions were limited in terms of relevant theories and computational approaches. More rigorous theories (e.g., linear elastic fracture mechanics [LEFMs] and Green's function-based elastic relationships) and approaches (e.g., the displacement discontinuity method [DDM]) applied to the theoretical study of hydraulic fracturing in the past two decades (Adachi & Detournay, 2002, 2008; Bunger et al., 2005; Chen, Barron, et al., 2018; Lu et al., 2020) have not been employed to theoretically study subsurface thermal fracturing.

Many thermo-hydro-mechanical (THM) simulators have been developed and used to model the coupled THM effects in the presence of fluid and pressure plumes often on the scale of km to hundreds of km (Goodarzi

et al., 2012; Liu et al., 2018; Salimzadeh et al., 2016; Salimzadeh, Paluszny, et al., 2018; Vilarrasa et al., 2014). Such general modeling studies focus on long-term effects of thermal stresses and fracturing and may underestimate the ΔT plume and fracturing region near injection wells for short-term injection because of strong grid effects. The grid effects were shown in Rangriz Shokri et al. (2019) by comparing modeling results with and without local mesh refinement around the injection well. In the latter, the simulated ΔT and thermal stresses were not sufficient to initiate fracturing, contradicting field observations of thermal fracturing at the Aquistore, Canada site. Salimzadeh, Paluszny, et al. (2018) focused on the growth of fracture length and aperture induced by cold CO_2 injection and found a significant increase in fracture aperture caused by near-well reservoir cooling. However, it is still a challenge for THM simulators to efficiently model decameter-scale near-well ΔT plume and fracturing region and km-scale fluid and pressure plumes and accurately account for the coupled THM-fracturing processes. This is particularly true when interpreting field phenomena (e.g., enhanced injectivity and flow focusing) observed at specific injection sites.

1.4. Modeling of Thermal Shock Fracturing

On the other hand, thermal shock fracturing, a common phenomenon in natural processes and engineered structures under no confining stress, has been investigated to better understand the initiation and propagation of thermal fractures induced by sudden temperature changes (Bahr et al., 1996, 2010). Critical to propagation of multiple thermal fractures is *fracture arrest* that results in dynamic fracture spacing and hierarchical fracture patterns. The fracture arrest has been investigated using the principle of energy minimization or stability analysis. The former solves for fracture length and spacing through minimizing the total energy, the sum of strain energy and fracture surface energy, in the system at a given time (Hasselman, 1963; Jiang et al., 2012). The strain energy is normally computed using approximation equations (Nemat-Nasser et al., 1978; Nemat-Nasser & Oranratnachai, 1979; Tarasovs & Ghassemi, 2014) or numerical methods (Jenkins, 2005), while the fracture surface energy is computed by the product of fracture length and energy release rate. The stability analysis was first introduced to study thermal shock fractures by Nemat-Nasser et al. (1978) and Nemat-Nasser et al. (1980). A criterion based on the stress intensity factor was used to check whether fracture arrest occurs or not and solve for the position of the occurring arrest. The stress intensity factor in the fracture-arrest criterion is normally calculated using numerical approaches, such as finite element method (FEM) and boundary element method (BEM) (Bahr et al., 1996). With this criterion, Bahr et al. (1996) solved with BEM for the relationship between fracture length and spacing in a dimensionless form over a large time range (Bahr et al., 2010). Chen and Zhou (2021) found the reactivation of initially arrested thermal fractures and derived a new relationship between fracture length and spacing in a dimensionless form.

Various numerical models have also been used for modeling thermal shock fracturing, including damage-based models (Tang et al., 2016, 2020), phase-field models (Chu et al., 2017; Miehe et al., 2015), particle-based discrete element method (DEM) models (Huang et al., 2016), and BEM models (Tarasovs & Ghassemi, 2014). However, most of the simulations (e.g., Chu et al., 2017; Tang et al., 2020) focused on thermal effects and fracturing under a specific set of material properties and conditions. Few modeling studies discussed the general mechanisms and phenomena of thermal fracturing. For example, the DEM modeling by Huang et al. (2016) showed that the maximum length of multiple interacting, propagating thermal fractures is linearly related to the square root of cooling time. The BEM modeling with randomly initiated fractures by Tarasovs and Ghassemi (2014) indicated an explicit relationship between normalized fracture length and spacing and normalized cooling depth obtained through power-law fitting of their numerical results. However, more comprehensive scaling behavior of fracture length, spacing, and aperture need to be investigated.

1.5. Objectives

For the subsurface applications mentioned above, there are different scenarios of thermal fracturing (see Figure 1), including (a) secondary, transverse (i.e., *half-plane*) thermal fractures initiated at the surfaces of hydraulic fractures or other fluid channels and driven by heat conduction into the low-permeability rock matrix (Enayatpour et al., 2019; Murphy, 1978), (b) *radial*, transverse thermal fractures initiated at horizontal wells and driven by radial heat conduction in the rock matrix in response to constant or cyclic wellbore cooling (Raterman et al., 2018, 2019), (c) *longitudinal* fractures initiated at vertical wells and driven by radial heat conduction (Brudy & Zoback, 1999), and (d) thermal fractures driven by convective-conductive heat transfer in the newly

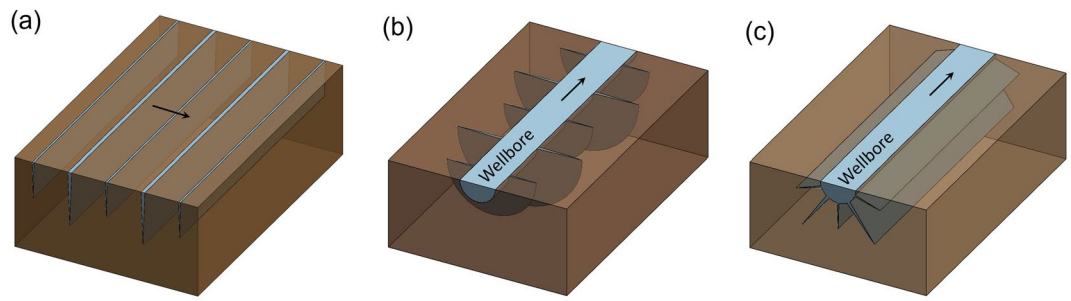

Figure 1. Different scenarios of thermal fracturing in deep formations: (a) half-plane thermal fractures driven by heat conduction from a cooling surface (e.g., a hydraulic fracture or fluid channel), (b) radial thermal fractures, and (c) longitudinal thermal fractures driven by radial heat conduction around a wellbore. The directions of fluid flow are indicated by black arrows.

created thermal fractures and the permeable rock matrix (Rangriz Shokri et al., 2019; Zhou et al., 2020). For the first three scenarios, heat convection in the rock and created thermal fractures is negligible for injection through *cased* well sections or injection through/into low-permeability rock (e.g., hot crystalline rock and unconventional shale), leading to simplified modeling. In all four scenarios, cooling-induced thermal stress is the dominant driving force for fracture propagation.

Our objectives are to theoretically address the different types of thermal fracturing in subsurface applications. To achieve these goals, we (a) combine the advanced modeling theories and approaches for thermal shock fracturing (e.g., the stability analysis) and hydraulic fracturing (e.g., scaling analysis and DDM), (b) obtain dimensionless solutions and late-time generic scaling behavior of fracture length, spacing, and aperture, (c) better understand the underlying mechanisms (i.e., inter-fracture stress interaction and fracture arrest), by comparing solutions of single fractures, constantly spaced multiple fractures (without arrest), and dynamically spaced multiple fractures (with arrest), and (d) systematically investigate the propagation and arrest of thermal fractures in deep formations under injection/flow conditions. For the first three scenarios with negligible heat convection (see Figure 1), the obtained dimensionless solutions are profiles for fracture spacing, length, and aperture, as a function of *one to three* dimensionless model parameters that cover the entire spectrum of rock properties, in situ confining stress, fluid pressure, and cooling conditions, as well as wellbore radius. In contrast, numerous simulations using traditional numerical simulators are needed for different combinations of the properties and conditions.

In this study, we focus on the first scenario (Figure 1a) with one-dimensional heat conduction and negligible heat convection using a plane strain model. The study is organized as follows. First, the governing equations for heat conduction and thermoelastic deformation and the criteria for fracture propagation and arrest are given and converted to their dimensionless counterparts using scaling analysis in Section 2. Second, the dimensionless solutions and scaling laws of single thermal fracture (Case A), constantly spaced multiple fractures (Case B), and dynamically spaced multiple fractures (Case C) are presented in Section 3. These solutions are compared to show the effects of inter-fracture stress interaction and fracture arrest. The associated methodologies for the analytical solution for Case A and for the DDM discretization and solution procedures and algorithms for Cases B and C are detailed in Appendices. Third, the verification of the dimensionless solutions using a FEM-based fracture model and the application of the Case C solution to a real-world geothermal reservoir to predict the evolution and pattern of thermal fractures are given in Section 4. Finally, the validity of the assumptions and simplifications used in the theoretical analysis is discussed in Section 5.

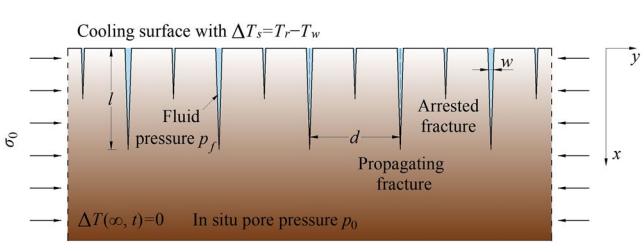

Figure 2. Schematic of propagation and arrest of thermal fractures of length l, spacing d, and aperture profile w, initiated at the surface with a cooling of ΔT_s and fluid pressure of p_f in a half-plane, under in situ confining stress of σ_0 and pore pressure of p_0 (modified from Chen and Zhou [2021]).

2. Problem Formulation and Governing Equations

We are interested in the thermal fracturing of a 2-D half-plane bounded by a surface that represents a primary hydraulic fracture or fluid channel in a low-permeability reservoir (Enayatpour et al., 2019; Murphy, 1978). In the plane strain model shown in Figure 2, the half-plane extends infinitely in the

x direction and sufficiently long in the y direction parallel to the surface and is subject to a uniform, in situ confining stress (or far-field stress), σ_0, in the y direction. Initially, the half-plane is of uniform in situ pore pressure p_0 and temperature T_r. A lower temperature of T_w is instantaneously introduced at the surface ($x = 0$) at time $t = 0$ and maintained constant over $t \geq 0$. This boundary condition represents a fluid of temperature T_w and pressure p_f ($\geq p_0$) circulates through the primary hydraulic fracture or flows through the fluid channel, while the temperature at $x = \infty$ remains at T_r. We are interested in strong surface cooling ($\Delta T_s = T_r - T_w$) so that high thermal stresses can initiate multiple thermal fractures at the surface. As observed in laboratory experiments (Bahr et al., 1986; Geyer & Nemat-Nasser, 1982; Shao et al., 2011), the thermal fractures commonly initiate and propagate in the direction perpendicular to the cooling surface due to more significant contraction along the direction of the surface. With heat transfer in the half-plane, some of the initiated fractures (referred to as propagating fractures) continue to propagate, while the others (referred to as arrested fractures) are arrested at different time and distance from the surface, leading to dynamically spaced multiple fractures and a hierarchical fracture pattern (Bahr et al., 1986; Geyer & Nemat-Nasser, 1982; Shao et al., 2011). This fracture pattern can be attributed to stress interaction between propagating fractures. (Note that the thermal fractures are hydraulically connected with the hydraulic fracture/channel at the surface, all with fluid pressure p_f.) The solutions of the problem include the evolution of the length ($l(t)$), spacing ($d(t)$), and aperture profile ($w(x, t)$) of all thermal fractures, as well as the pattern of arrested and propagating fractures at different times.

The coupled problem with fracture propagation and arrest, thermoporoelasticity, heat transfer (convection and conduction), and fluid flow in the fractures and reservoir can be solved numerically only. To make the problem tractable theoretically, we make the following assumptions:

1. The rock matrix is assumed to be impermeable with no fluid flow. Heat convection by fluid flow in the thermal fractures is negligible in comparison with heat conduction through the rock matrix from the cooling surface. (As shown by Salimzadeh, Nick, et al. [2018], heat convection has a negligible effect on the temperature distribution for rock permeability less than 10^{-17} m^2.) The reservoir is homogeneous and isotropic for heat conduction, not affected by thermal fractures (because of the difference between their aperture and spacing); the analytical solution of temperature available can be used to calculate thermal stress. This assumption of homogeneity and isotropy is commonly used for deriving analytical solutions in subsurface hydrology (Cihan et al., 2011; Zhou et al., 2019).
2. In the 2-D plane strain model used (not fully 3-D), propagating thermal fractures are equally spaced at any time and fracture arrest occurs alternately, leading to the mode-I propagation. Fracture propagation and arrest are controlled only by the stresses in the mechanically homogeneous half-plane assumed by neglecting microscale rock heterogeneities and mesoscale joints. These lead to an idealized hierarchical pattern of dynamically spaced thermal fractures that is not far from those observed in laboratory experiments of thermal shock fractures. This plane strain assumption is commonly used for analyzing thermal shock fracturing (Bahr et al., 2010; Murphy, 1978).
3. Only thermal fractures under cooling-induced thermal stress and fluid pressure p_f in the fractures are modeled. The pressure is not sufficient to create new hydraulic fractures so that the thermal stress is the driving force of thermal fracturing. The hydraulic fracture (i.e., the cooling surface), considered as a symmetric boundary, is not modeled.
4. The reservoir is a porous medium saturated with water. The initial stress state with in situ confining stress σ_0, fluid pressure p_0, and temperature T_r before fluid circulation and reservoir cooling can be described by far-field effective stress $\sigma_e = \sigma_0 - p_0$ at the two side boundaries using Terzaghi's effective stress principle (Cheng, 2016; Terzaghi, 1936). This boundary condition of σ_e is used in our modeling.
5. During fluid circulation and reservoir cooling, the fluid pressure in the hydraulic fracture and thermal fractures p_f ($\geq p_0$) is constant with time and uniformly distributed (because of the large time scale of thermal fracturing and small flow rate through the thermal fractures) (Brudy & Zoback, 1999; Rummel & Hansen, 1989), leading to a pressure increase in thermal fractures $\Delta p = p_f - p_0$. By neglecting the effects of thermoporoelasticity (Rummel & Hansen, 1989), we define an effective confining stress $\sigma_{ec} = \sigma_e - \Delta p = \sigma_0 - p_f$. It is this effective confining stress, along with thermal stress and inter-fracture stress interaction, that controls the propagation and arrest of thermal fractures.

The validity of the first two assumptions is discussed in Section 5. The last two assumptions are valid for a porous but impervious formation with uniform pore pressure, as used for estimating the breakdown pressure in

a wellbore (Hubbert & Willis, 1957; Jaeger et al., 2007; Schmitt & Zoback, 1989a, 1989b). For example, the Terzaghi effective stress $\sigma_e = \sigma_0 - p_0$ at the far field and $\Delta p = p_f - p_0$ on the internal boundary of a wellbore were used (Hubbert & Willis, 1957; Zoback, 2007). For a porous and permeable formation, there are thermoporoelastic effects on fracture propagation and arrest that need to be considered. The Δp-induced poroelastic effect around a drilled wellbore was estimated analytically using the Biot's theory of poroelasticity (Detournay & Cheng, 1988, 1993). Such a poroelastic effect on hydraulic fractures was also shown by comparing numerical results with semi-analytical solutions developed based on the linear elasticity (Gao & Ghassemi, 2020; Salimzadeh et al., 2017). The cooling-induced poroelastic effect includes a pressure decrease caused by more contraction of water than solid grains (with a smaller thermal expansion coefficient) (Cheng, 2016; McTigue, 1986). The two poroelastic effects (i.e., injection-induced pressure increase and cooling-induced pressure decrease) are compensated to a certain degree in a thermoporoelastic rock mass. These effects depend on rock properties, such as porosity, permeability, the Biot coefficient for poroelasticity, and thermal properties (Cheng, 2016; Jaeger et al., 2007; McTigue, 1986; Salimzadeh, Nick, et al., 2018; Schmitt & Zoback, 1989b). The thermal properties do not vary considerably among different rocks. However, the wide ranges of rock porosity (less than 1%–40%), permeability (10^{-21} to 10^{-9} m^2), and the Biot coefficient (0–1) can have critical influences on the thermoporoelastic effects (Salimzadeh, Nick, et al., 2018). We limit our study to a low-permeability, low-porosity crystalline rock, or low-permeability unconventional shale that are of interest to many applications; in the cases, the Biot coefficient is often small and the resultant thermoporoelastic effect is expected to be relatively small.

2.1. Governing Equations

For the problem with the above assumptions shown in Figure 2, the coupled thermo-mechanical-fracturing (TMF) processes are governed by the heat conduction equation, the elastic equilibrium equation for stresses induced by cooling and fracturing (as well as the effective confining stress), and the criteria for fracture propagation and arrest. The following governing equations differ from those in Chen and Zhou (2021) by introducing the effective confining stress σ_{ec} for subsurface applications as discussed above.

2.1.1. Heat Conduction and Thermal Stress

The governing equation for one-dimensional heat conduction (Carslaw & Jaeger, 1959) is written

$$\frac{\partial^2 T}{\partial x^2} = \frac{1}{D}\frac{\partial T}{\partial t} \tag{1}$$

where x is the distance from the cooling surface, D is the thermal diffusivity calculated by $D = \lambda/\rho c$, λ is the thermal conductivity, ρ is the rock density, and c is the specific heat capacity at constant pressure.

The solution of Equation 1 for the transient temperature change, $\Delta T(x,t)$, in the half-plane, with initial condition $\Delta T(x,0) = 0$ and boundary conditions $\Delta T(0,t) = \Delta T_s$ and $\Delta T(\infty,t) = 0$, is available in the literature (Carslaw & Jaeger, 1959). $\Delta T(x,t)$ is calculated by

$$\Delta T(x,t) = \Delta T_s erfc\frac{x}{2\sqrt{Dt}} \tag{2}$$

where erfc() is the complementary error function.

The thermally induced stress in the y direction in the half-plane (Bažant et al., 1979; Tarasovs & Ghassemi, 2011, 2014) is calculated by

$$\sigma_{\Delta T}(x,t) = \frac{E}{(1-\nu)}\beta\Delta T(x,t) \tag{3}$$

where E is the Young's modulus of the rock, ν is the Poisson's ratio, and β is the linear thermal expansion coefficient. The thermal stress is applied on the surfaces of thermal fractures in the elasticity equation according to the superposition principle.

2.1.2. Elasticity Equation

In addition to the cooling-induced thermal stress ($\sigma_{\Delta T}$), as well as the effective confining stress (σ_{ec}), we have to consider the stress induced by the fracture of interest, located at the center of the plane ($y = 0$) and referred to as the center fracture, and stress interaction between the center fracture and all other fractures located at $y = \pm k'd \quad (k' = 1, \ldots \infty)$. We can write the elastic equilibrium equations for this fracture (X. Zhang et al., 2009; Z. Zhang et al., 2015):

$$\sum_{k=1}^{\infty} \int_0^{l_k} [g_{NS}(x,s)u(s,t) + g_{NN}(x,s)w(s,t)]\, ds = \sigma_{\Delta T}(x,t) - \sigma_{ec} \tag{4a}$$

$$\sum_{k=1}^{\infty} \int_0^{l_k} [g_{SS}(x,s)u(s,t) + g_{SN}(x,s)w(s,t)]\, ds = 0 \tag{4b}$$

where k is the fracture index that ranges over all the fractures, subscripts N and S denote the normal direction (the y direction) and the shear direction (the x direction) respectively, g_{NS}, g_{NN}, g_{SS}, and g_{SN} are the hyper singular Green's functions (Crouch & Starfield, 1983), u is the shear displacement and w is the normal displacement (i.e., fracture aperture).

The fracture pattern of interest in this study is always symmetric along any thermal fracture (see the second assumption above). Therefore, the shear displacement is zero, leading to a simplified form of Equations 4a and 4b as follows

$$\sum_{k=1}^{\infty} \int_0^{l_k} g_{NN}(x,s)w(s,t)ds = \sigma_{\Delta T}(x,t) - \sigma_{ec} \tag{5}$$

2.1.3. Criterion for Fracture Propagation

It is assumed that fracture propagation is quasistatic and governed by the LEFM. Since the LEFM theory cannot simulate fracture initiation in intact rock, initial fractures with very small length are needed to start the analysis of this study. The fracture propagation criterion is that the stress intensity factor (K_{I}) equals the rock toughness (K_{Ic}):

$$K_{\mathrm{I}} = K_{\mathrm{Ic}} \tag{6}$$

For multiple thermal fractures, the stress intensity factor for each fracture is computed according to the asymptote of fracture aperture near the fracture tip. Based on the LEFM theory, the following condition (Lecampion & Detournay, 2007; Rice, 1968) holds

$$w(x) \to \sqrt{\frac{32}{\pi}} \frac{\left(1 - \nu^2\right)\sqrt{l - x}K_{\mathrm{I}}}{E}, \quad \text{for} \quad x \to l \tag{7}$$

Although the elasticity equation, Equation 5, and the fracture propagation criteria, Equations 6 and 7, are static or quasistatic, they are coupled with the transient temperature solution in Equation 2 through thermal stress given in Equation 3. This observation is useful for deriving scaling laws for late-time fracture propagation using variable separation. In addition, Equations 6 and 7 need to be solved together with Equation 5 at each time step for computing the fracture aperture and length, both of which depend on effective confining stress σ_{ec} and thus fluid pressure in the fractures.

2.1.4. Stability Analysis for Fracture Arrest

In addition to fracture propagation, we also need to consider fracture arrest caused by inter-fracture stress interaction. For multiple fractures with a specific spacing, a condition of instability, under which some fractures are arrested, occurs during fracture propagation. The stability analysis (Bahr et al., 2010; Hofmann et al., 2011; Nemat-Nasser et al., 1980) is used to find the critical fracture length corresponding to the fracture arrest. We divide equally spaced fractures with identical length into two fracture subsets: subset A with length l_A for every other fracture remaining propagating and subset B with length l_B for other fractures to be arrested. The instability condition (Bahr et al., 2010; Chen & Zhou, 2021; Hofmann et al., 2011; Nemat-Nasser et al., 1978, 1980) in the case of $dl_A > 0, \quad dl_B = 0$ is expressed by

$$\frac{\partial K_A}{\partial l_A} - \frac{\partial K_B}{\partial l_A} > 0 \tag{8}$$

where K_A and K_B are the stress intensity factors of fractures in subset A and subset B, respectively.

This instability condition implies that a minimum extension of fractures in subset A facilitates their propagation and retards fractures in subset B. (In reality, such an unequal fracture length may be caused by a perturbation due to rock heterogeneity or non-uniform fracture spacing.) The condition is checked in the modeling by artificially extending subset A fractures by a certain length (e.g., $dl_A \approx 0.01 l_A$) while fixing the thermal stress field, and then solving for K_A and K_B. Note that the stability analysis provides an efficient way to theoretically model dynamically spaced thermal fractures and the assumption of equally spaced fractures is needed to facilitate the analysis. In addition, for a large number of equally spaced fractures, the selection of propagating and arrested fractures does not affect the fracture pattern predicted because of their alternating nature.

2.2. Dimensionless Governing Equations

To focus on the scaling behavior of thermal fractures, we introduce dimensionless variables that group diverse rock properties, in situ conditions, and boundary conditions shown in Equations 2 through 8. A similar scaling analysis has been extensively used for semi-analytical modeling of hydraulic fractures (Adachi & Detournay, 2002; Bunger et al., 2005; Chen, Barron, et al., 2018; Lecampion & Detournay, 2007; Lu et al., 2017).

For a single thermal fracture in the half-plane, the stress intensity factor (Chen, Barron, et al., 2018; Lecampion & Detournay, 2007) is computed by

$$K_{\mathrm{I}} = 2\sqrt{\frac{l}{\pi}} \int_0^l \frac{\sigma_{\Delta T} - \sigma_{ec}}{\sqrt{l^2 - x^2}} dx \tag{9}$$

Substituting Equations 2, 3, and 6 into Equation 9 leads to the governing equation for propagation of single thermal fracture:

$$\frac{(1-v)K_{\mathrm{Ic}}}{2E\beta\Delta T_s} = \sqrt{\frac{l}{\pi}} \int_0^1 \frac{1}{\sqrt{1-\xi^2}} \mathrm{erfc}\left(\frac{\xi l}{2\sqrt{Dt}}\right) d\xi - \frac{(1-\nu)\pi\sigma_{ec}}{2E\beta\Delta T_s}\sqrt{\frac{l}{\pi}} \tag{10}$$

where $\xi = x/l$.

Following a preliminary analysis of Equation 10, we introduce dimensionless fracture length ($\mathcal{L}$), dimensionless distance ($\mathcal{X}$), dimensionless time (τ), and dimensionless effective confining stress ($\mathcal{T}$) for their corresponding l, x, t, and σ_{ec}, respectively:

$$\mathcal{L} = l\left(\frac{E\beta\Delta T_s}{(1-\nu)K_{\mathrm{Ic}}}\right)^2, \quad \mathcal{X} = x\left(\frac{E\beta\Delta T_s}{(1-\nu)K_{\mathrm{Ic}}}\right)^2 \quad \tau = Dt\left(\frac{E\beta\Delta T_s}{(1-\nu)K_{\mathrm{Ic}}}\right)^4, \quad \mathcal{T} = \frac{\sigma_{ec}(1-\nu)}{E\beta\Delta T_s} \tag{11}$$

After the introduction of these dimensionless variables, Equation 10 is rewritten

$$\sqrt{\frac{4\mathcal{L}}{\pi}}\left(\int_0^1 \frac{1}{\sqrt{1-\xi^2}} \mathrm{erfc}\left(\frac{\mathcal{L}}{2\sqrt{\tau}}\xi\right) \mathrm{d}\xi - \frac{\pi}{2}\mathcal{T}\right) = 1 \tag{12}$$

For multiple fractures, we also introduce dimensionless fracture spacing ($\mathcal{D}$) (scaled in the same form as $\mathcal{L}$)

$$\mathcal{D} = d\left(\frac{E\beta\Delta T_s}{(1-\nu)K_{\mathrm{Ic}}}\right)^2 \tag{13}$$

and dimensionless fracture aperture profile ($\Omega(\mathcal{X}, \tau)$)

$$\Omega = w\frac{E^2\beta\Delta T_s}{(1-\nu^2)(1-\nu)K_{\mathrm{Ic}}^2} \tag{14}$$

Note that Ω is easily defined according to Equations 6 and 7 and $\mathcal{L}$ in Equation 11 with constants not included.

The dimensionless elasticity equation for multiple thermal fractures is derived by substituting Equations 2 and 3 into Equation 5 and applying the dimensionless variables in Equations 11, 13, and 14, and written:

$$\sum_{k=1}^{\infty} \int_0^{\mathcal{L}_k} [G_{NN}(\mathcal{X}, \mathcal{S})\Omega(\mathcal{S}, \tau)]\, d\mathcal{S} = \operatorname{erfc}\left(\frac{\mathcal{X}}{2\sqrt{\tau}}\right) - \mathcal{T} \tag{15}$$

where $\mathcal{T}$ is the additional term compared to the dimensionless elasticity equation in Chen and Zhou (2021) for non-confinement applications.

Similarly, the dimensionless fracture propagation criterion is derived by substituting Equation 6 into Equation 7 and applying the dimensionless variables, and written:

$$\Omega \to \sqrt{\frac{32\mathcal{L}}{\pi}}\ \sqrt{1-\xi}, \quad \text{for} \quad \xi \to 1 \tag{16}$$

For fracture arrest, the instability condition, Equation 8, is converted to its corresponding dimensionless form (see Equation C4 in Appendix C) after numerical discretization using the above dimensionless variables.

3. Dimensionless Solutions and Scaling Laws

We are interested in the dimensionless solutions of dynamically spaced multiple thermal fractures (Case C) to predict transient fracture length, spacing, and aperture for real subsurface problems. A better understanding of the effects of inter-fracture stress interaction and fracture arrest is also of interest; the dimensionless solutions of single thermal fracture (Case A) and constantly spaced multiple thermal fractures (without arrest; Case B) are thus developed. The solution comparison between Cases A and B shows the effect of fracture spacing (i.e., different degree of inter-fracture stress interaction) on the evolution of fracture length, while that between Cases B and C shows the effect of fracture arrest on all fracture properties (length, spacing, aperture, and pattern). These transient solutions and related scaling laws for late-time fracture propagation are detailed in Section 3.2. The corresponding solution approaches are briefly summarized in Section 3.1, while the details of the theoretical developments are given in the Appendices.

3.1. Solution Approaches

The thermal fracturing in Cases A through C is solved using an analytical or numerical approach depending on their complexities. In Case A, the propagation of single fracture is solely governed by Equation 12. The transient solution of dimensionless fracture length $\mathcal{L}(\tau, \mathcal{T})$ for a given dimensionless effective confining stress $\mathcal{T}$ is derived analytically (see Appendix A1). In Case B, the propagation of constantly spaced multiple thermal fractures is governed by Equations 15 and 16 that are coupled through $\mathcal{L}(\tau, \mathcal{T}, \mathcal{D})$ and $\Omega(\tau, \mathcal{T}, \mathcal{D})$. The two equations are discretized using DDM and solved iteratively during each time step (see Appendix B). The corresponding solutions depend on two model parameters, $\mathcal{T}$ and $\mathcal{D}$.

In Case C, an additional equation (Equation C4 in Appendix C), the dimensionless counterpart of Equation 8, is needed to determine the critical state of fracture arrest. Equations 15, 16, and C4 are coupled, and two special algorithms are developed to model fracture propagation and arrest that lead to the classic hierarchical fracture pattern (see Figure 2), by following the theoretical development for the case of no confinement in a previous study (Chen & Zhou, 2021). The first algorithm is used to determine the critical states at fracture arrests (arrest line, denoted as $(\tau_a, \mathcal{L}_a, \Omega_a, \mathcal{D}_a)$) for any given values of fracture spacing, as well as the approximate solution with continuous fracture spacing assumed (central line, denoted as $(\tau_o, \mathcal{L}_o, \Omega_o, \mathcal{D}_o)$), where subscripts a and o represent the solutions at the arrest line and the central line, respectively, and Ω_a and Ω_o are the vectors of the discretized dimensionless aperture along the thermal fracture at the states of arrest line and central line, respectively (see Appendix C). The arrest and central lines provide fast predictions of evolution of fracture length, spacing, and aperture. The second algorithm is used to obtain the fully transient solution with stepwise fracture spacing $(\mathcal{D}_0, 2\mathcal{D}_0, 4\mathcal{D}_0, \ldots)$ and continuous fracture length, as well as fracture pattern, with $\mathcal{D}_0$ being a specified initial spacing (see Appendix C).

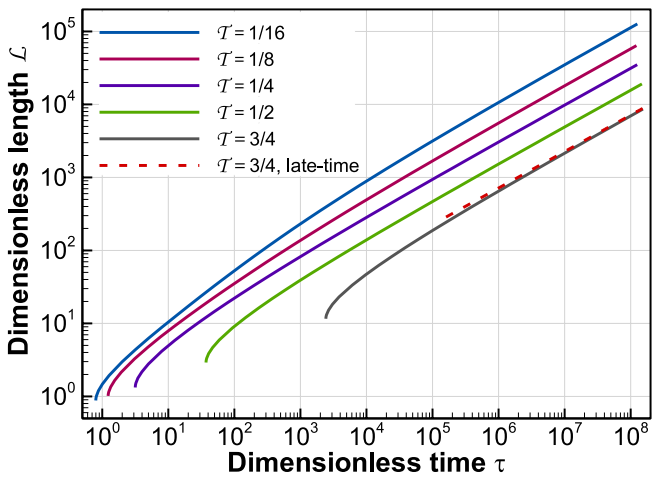

Figure 3. Evolution of dimensionless fracture length $\mathcal{L}$ of single thermal fracture with dimensionless time τ for different dimensionless effective confining stress $\mathcal{T}$.

The transitions from Case A solution to Case B solution and to Case C solution are clearly illustrated when putting all solutions together in Figure C1b. The computer codes used for all the modeling for a given $\mathcal{T}$ value are available in the data (see Acknowledgments).

3.2. Results of Solutions and Scaling Laws

This section focuses on the results of single thermal fracture (Section 3.2.1), multiple constantly spaced thermal fractures (Section 3.2.2), and multiple dynamically spaced thermal fractures (Section 3.2.3). The results are general profiles of fracture properties (e.g., dimensionless fracture length) as functions of dimensionless time τ and dimensionless effective confining stress $\mathcal{T}$, which represents various reservoir and cooling conditions.

3.2.1. Single Thermal Fracture

Figure 3 shows the evolution of dimensionless fracture length $\mathcal{L}$ with dimensionless time τ during stable propagation for five different $\mathcal{T}$ values, calculated using the developed analytical solution (Appendix A1). For a given $\mathcal{T}$, $\mathcal{L}$ starts from the critical state $[\tau_c, \mathcal{L}_c]$, increases nonlinearly with $\sqrt{\tau}$, and transitions to a linear increase with $\sqrt{\tau}$. $\mathcal{L}$ also decreases with the increase in $\mathcal{T}$ at any τ, indicating that single thermal fracture propagates at a slower speed under higher dimensionless effective confining stress.

For late-time fracture propagation under finite dimensionless effective confining stress (i.e., $\mathcal{T} > 0$, $\tau \to \infty$ and $\mathcal{L} \to \infty$), the dimensionless governing equation for single thermal fracture, Equation 12, can be further simplified to Equation A1. As derived in Appendix A2, the late-time dimensionless fracture length $\mathcal{L}$ satisfies

$$\mathcal{L} = f(\mathcal{T})\sqrt{\tau} \tag{17}$$

where $f(\mathcal{T})$ is the scaling coefficient dependent only on $\mathcal{T}$. In this scaling law, $\mathcal{L}$ is linear with $\sqrt{\tau}$, with the effect of $\mathcal{T}$ fully separated from that of τ.

The asymptotic solutions of scaling coefficient $f(\mathcal{T})$ in the limiting cases $\mathcal{T} \to 0$ and $\mathcal{T} \to 1$ are also derived

$$f(\mathcal{T}) = \begin{cases} 4/\left(\pi^{3/2}\mathcal{T}\right) & \mathcal{T} \to 0 \\ \pi^{3/2}(1-\mathcal{T})/2 & \mathcal{T} \to 1 \end{cases} \tag{18}$$

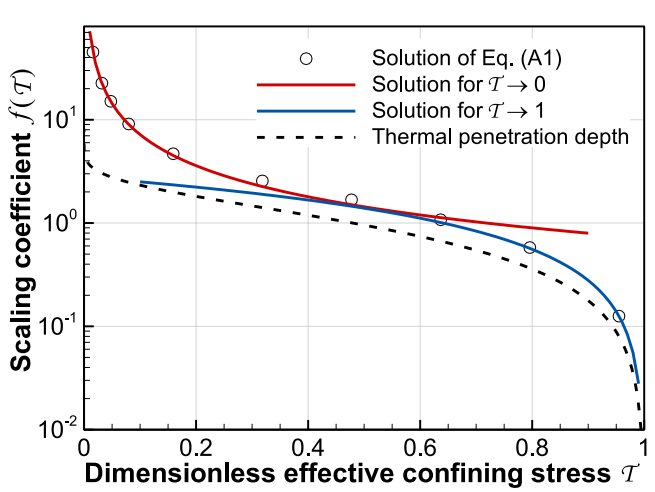

Figure 4. Dependence of scaling coefficient $f(\mathcal{T})$ on dimensionless effective confining stress $\mathcal{T}$ for late-time propagation of single thermal fracture, compared with the coefficient of thermal penetration distance.

For an arbitrary $0 < \mathcal{T} < 1$, $f(\mathcal{T})$ is obtained by solving Equation A1 (see Figure 4). The obtained $f(\mathcal{T})$ approaches to the solution in Equation 18 for $\mathcal{T}$ close to 1 or 0. Indeed, the asymptotic solution for $\mathcal{T} \to 0$ is valid for $0 < \mathcal{T} < 0.25$ with a maximum error less than 10%, and the asymptotic solution for $\mathcal{T} \to 1$ is valid for $0.5 < \mathcal{T} < 1$ with a maximum error less than 10%. Figure 4 clearly shows that dimensionless fracture length is more sensitive to $\mathcal{T}$ for a smaller $\mathcal{T}$, as shown by the change of scaling coefficient $f(\mathcal{T})$ with $\mathcal{T}$.

Indeed, the scaling law in Equation 17, with the $f(\mathcal{T})$ value directly calculated using Equation 18 or interpolated from the solution of Equation A1 in Figure 4, can be used for fast prediction of dimensionless fracture length at late time for any given dimensionless effective confining stress. Moreover, the transition from the transient solution to the scaling law occurs relatively early (e.g., at $\tau = 10^6$ for $\mathcal{T} = 3/4$), as shown in Figure 3.

Using the definitions of dimensionless variables in Equation 11, Equation 17 can be rewritten

$$l = f(\mathcal{T})\sqrt{Dt} \tag{19}$$

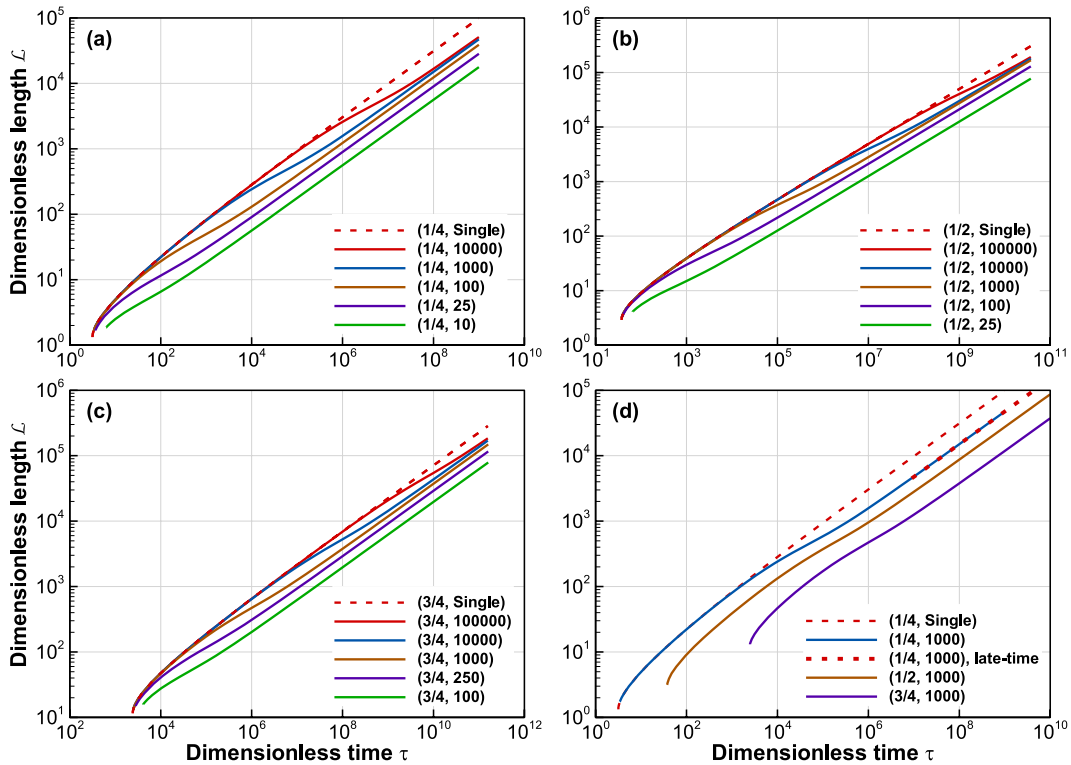

Figure 5. Evolution of dimensionless fracture length $\mathcal{L}$ with dimensionless time τ for the propagation of multiple thermal fractures with different spacing $\mathcal{D}$ under (a) $\mathcal{T} = 1/4$, (b) $\mathcal{T} = 1/2$, and (c) $\mathcal{T} = 3/4$, as well as (d) comparison between solutions with different $\mathcal{T}$ for $\mathcal{D} = 1000$.

This scaling law shown in Equation 17 or 19 indicates that (a) fracture length l linearly increases with the square root of cooling time t and (b) fracture length increases with the decrease in dimensionless effective confining stress in a more complicated way (see Figure 4) during the late-time propagation of single thermal fracture. It is of interest to observe that thermal penetration distance, defined here as the distance with thermal stress equal to effective confining stress (i.e., $\mathrm{erfc}(\mathcal{X}/2\sqrt{\tau}) = \mathcal{T}$), and the cumulative heat flux from the cooling surface to the half-plane (Zhou, Oldenburg, Rutqvist, et al., 2017; Zhou, Oldenburg, Spangler, et al., 2017) are also linear with $\sqrt{Dt}$. As shown in Figure 4, the corresponding coefficient of thermal penetration distance is smaller than $f(\mathcal{T})$, especially for small $\mathcal{T}$, and cannot be used to simply estimate fracture length, even though thermal stress is the driving force for fracture propagation. This indicates that the fracture front influenced by $\mathcal{T}$ and rock toughness needs to be solved as a fracture propagation problem instead of simply following the thermal front.

3.2.2. Constantly Spaced Thermal Fractures

The program in Appendix B is used to calculate the evolution of dimensionless fracture length with dimensionless time for a given pair of $(\mathcal{D}, \mathcal{T})$. Figure 5 shows the transient solutions of $\mathcal{L}$ for 15 pairs of $(\mathcal{D}, \mathcal{T})$ with three different $\mathcal{T}$ values. For a given $\mathcal{T}$, the $\mathcal{L}(\tau, \mathcal{D})$ solution deviates from the $\mathcal{L}(\tau)$ solution for single fracture at a later τ for a higher $\mathcal{D}$. After the deviation time, the $\mathcal{L}(\tau, \mathcal{D})$ solution is smaller than the $\mathcal{L}(\tau)$ solution, indicating that the stress interaction between fractures slows down fracture propagation. *The smaller $\mathcal{D}$ is, the stronger the stress interaction becomes, and the smaller $\mathcal{L}(\tau, \mathcal{D})$ is*. Before the deviation time, each of the multiple fractures behaves like a single fracture as stress interaction is negligible. In addition, the higher $\mathcal{T}$ is, the shorter $\mathcal{L}(\tau, \mathcal{D})$ is for a given τ (see Figure 5d). This indicates that multiple fractures propagate at a slower speed under a higher $\mathcal{T}$.

As shown in Figure 5d, the transient solution for a pair of $(\mathcal{D}, \mathcal{T})$ always approaches to a linear relationship between $\mathcal{L}$ and $\sqrt{\tau}$. Following the scaling law for single thermal fracture, Equation 17, we propose the following scaling law for the late-time propagation of multiple fractures with constant spacing:

$$\mathcal{L} = f(\mathcal{D}, \mathcal{T})\sqrt{\tau} \tag{20}$$

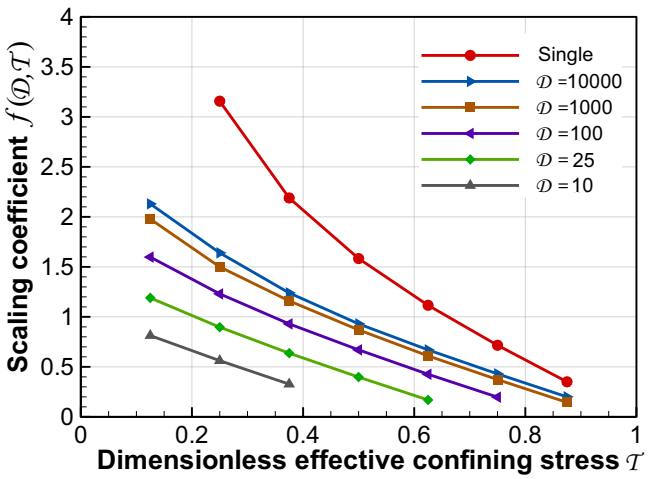

Figure 6. Dependence of scaling coefficient $f(\mathcal{D},\mathcal{T})$ on dimensionless effective confining stress $\mathcal{T}$ and fracture spacing $\mathcal{D}$ for late-time propagation of multiple constantly spaced thermal fractures.

where $f(\mathcal{D},\mathcal{T})$ is the scaling coefficient dependent on $\mathcal{D}$ and $\mathcal{T}$.

We fit the late-time transient solutions shown in Figure 5 against Equation 20 to obtain the value of the scaling coefficient for each pair of $(\mathcal{D},\mathcal{T})$. Figure 6 shows the dependence of the scaling coefficient on $\mathcal{D}$ and $\mathcal{T}$. Clearly, $f(\mathcal{D},\mathcal{T})$ decreases with the increase in $\mathcal{T}$ and the decrease in $\mathcal{D}$. More importantly, $f(\mathcal{D},\mathcal{T})$ for a large $\mathcal{D}$ is not as sensitive to $\mathcal{D}$ as a smaller $\mathcal{D}$. (This feature is used in analyzing the late-time propagation of dynamically spaced multiple fractures in Section 3.2.3.) These discrete coefficient values can be used to interpolate for the $f(\mathcal{D},\mathcal{T})$ value for any given $(\mathcal{D},\mathcal{T})$ and the scaling law in Equation 20 can be used to estimate dimensionless fracture length for late-time propagation. Note that the difference between the $f(\mathcal{D},\mathcal{T})$ for constantly spaced multiple fractures and $f(\mathcal{T})$ for single fracture is still large for $\mathcal{D} = 10,000$, especially for low $\mathcal{T}$.

3.2.3. Dynamically Spaced Thermal Fractures

As described in Section 3.1, the solutions of dynamically spaced thermal fractures include: (a) the critical states at fracture arrest (i.e., the arrest line separating the stable and unstable states), (b) the approximate solution with continuous fracture spacing assumed (the central line), and (c) the fully transient solution with stepwise spacing increased from a specified initial spacing. Only the arrest-line solution is discussed in this section, while the other two solutions are presented in Section 4.2.

Figure 7 shows the solutions (arrest lines) of dimensionless fracture length $\mathcal{L}$, spacing $\mathcal{D}$, and surface aperture Ω_0 (aperture at the cooling surface). A monotonic increase of $\mathcal{D}(\mathcal{X})$ for a given dimensionless effective confining stress is observed (Figure 7a). For $\mathcal{T} \geq 5/16$, $\mathcal{D}$ increases with $\mathcal{T}$ for any $\mathcal{X}$. For $\mathcal{T} < 5/16$, $\mathcal{D}$ increases with

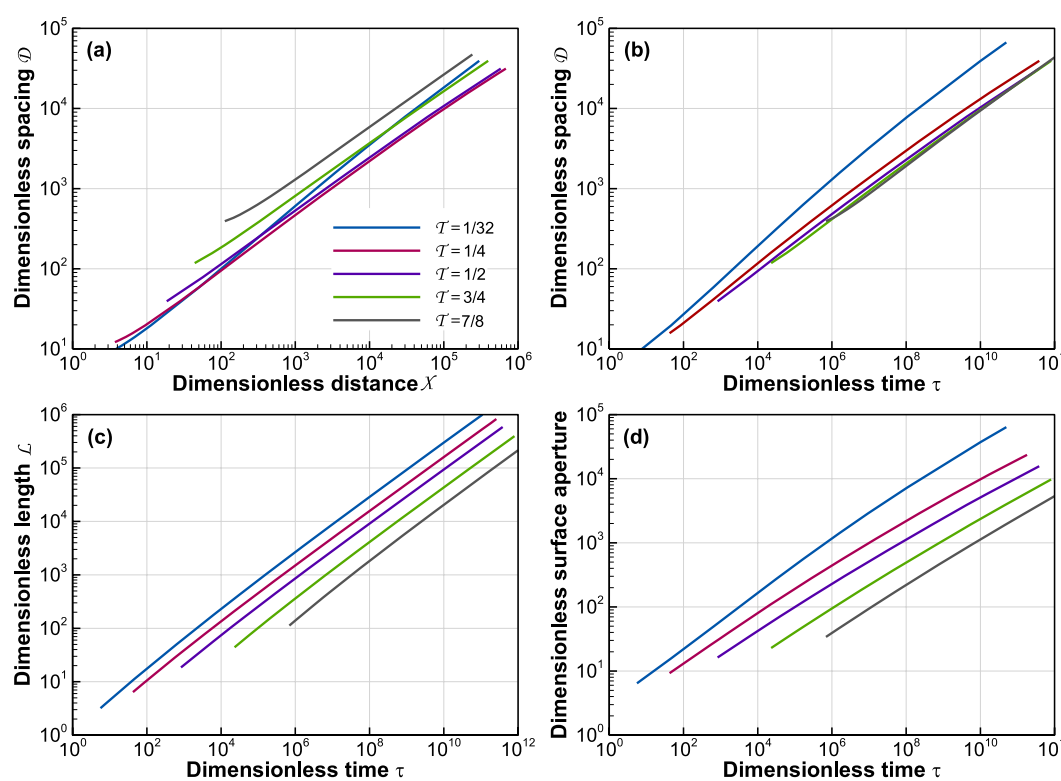

Figure 7. Evolution of dimensionless fracture spacing $\mathcal{D}$, length $\mathcal{L}$, and surface aperture Ω_0 under different dimensionless effective confining stress $\mathcal{T}$: (a) $\mathcal{D}(\mathcal{X})$, (b) $\mathcal{D}(\tau)$, (c) $\mathcal{L}(\tau)$, and (d) $\Omega_0(\tau)$.

Table 1
Rock Properties and In Situ Conditions at the Utah FORGE Site (EGI, 2019; Robertson, 1988)

Properties and initial conditions	Labels	Values
Young's modulus	E	55 GPa
Poisson's ratio	ν	0.26
Density	ρ	2,750 kg/m^3
Fracture toughness	K_{Ic}	2.48 MPa·m$^{1/2}$
Thermal conductivity	λ	3.05 W/(m·K)
Specific heat capacity	c	790 J/(kg·K)
Thermal diffusivity	D	1.40×10^{-6} m^2/s
Linear thermal expansion coefficient	β	8.0×10^{-6} K^{-1}
Reservoir temperature	T_r	200°C
Boundary temperature	T_w	50°C
Confining stress	$[\sigma_x, \ \sigma_y]$	[40.0, 32.2] MPa
Fluid pressure	p_f	22.5 MPa

increase in $\mathcal{T}$ for $\mathcal{X} < 100$ and with decrease of $\mathcal{T}$ for $\mathcal{X} > 100$. Note that a specific $\mathcal{X}$ (i.e., $\mathcal{L}$) is reached at earlier time for a smaller $\mathcal{T}$ (see Figure 7c). In addition, it is observed that $\mathcal{L}$ is up to 1 order of magnitude larger than $\mathcal{D}$ for large τ, while they are on the same order of magnitude for small τ. This means propagating fractures tend to have a fracture length longer than spacing during late-time propagation. Figure 7b shows the monotonic increase of $\mathcal{D}(\tau)$ with τ for different $\mathcal{T}$ values so that we can compare dimensionless fracture spacing with the same thermal stress at a given time but different effective confining stress.

As shown in Figure 7c, the dimensionless length of propagating fractures increases with dimensionless time and approach to $\mathcal{L} = f'(\mathcal{T})\sqrt{\tau}$ with $f'(\mathcal{T}) = f(\mathcal{D}, \mathcal{T})|_{\mathcal{D}\to\infty}$ for late-time propagation, for which the dynamic effect of $\mathcal{D}(\tau)$ on $f(\mathcal{D}, \mathcal{T})|_{\mathcal{D}\to\infty}$ is negligible for large $\mathcal{D}(\tau)$ (see Figure 6). Before this stage, the effect of dynamic spacing decreases with increase in τ, and $\mathcal{L}(\tau)$ increases with $\sqrt{\tau}$ in a nonlinear form. For any given time with the same thermal stress distribution, dimensionless fracture length decreases with the increase in dimensionless effective confining stress. Compared with the solutions of a series of constant spacing, the dynamic-spacing solution for a given $\mathcal{T}$ shows faster fracture propagation after each arrest than the constant-spacing solution (with the spacing just before the arrest; Figure C1b). *After the arrest, fracture spacing is doubled, leading to weaker fracture interaction and increased fracture length.*

A similar conclusion can be made for dimensionless surface aperture of propagating fractures (see Figure 7d). The surface aperture increases with dimensionless time in a quasi-power law, with the exponent (i.e., the slope) slightly decreasing with time and similar for relatively high $\mathcal{T}$ values. At a given time, the surface aperture decreases with the increase in $\mathcal{T}$, which is understandable in the point of view of geomechanics. The exponent for a very small $\mathcal{T}$ is higher than that for higher $\mathcal{T}$ values, indicating that cooling can produce a larger fracture aperture in very shallow subsurface formations.

4. Validation and Application of the Developed Solutions

The analytical solution of single fracture and the dimensionless solutions of constantly and dynamically spaced multiple fractures presented in Section 3 (referred to hereafter as theoretical solutions) are first validated using a FEM-based fracture model. The solution of dynamically spaced fractures is then applied to several cases with elevated fluid pressure. For the validation and application, the rock properties and in situ conditions of pressure, temperature, and stresses from a geothermal site are used.

4.1. The FORGE EGS Site

Detailed site characterization has been conducted at the Milford, Utah EGS site dedicated for the Frontier Observatory for Research in Geothermal Energy (FORGE) (EGI, 2019). Table 1 lists the rock properties acquired from the Utah FORGE site and used in our modeling analyses. The in situ rock temperature measured at the depth of 2,297 m is 197°C. The in situ minimum horizontal stress at the depth measured using different methods is around 32.2 MPa. Two horizontal wells will be drilled as an injector and a producer and their laterals will be placed at the depth of ~2,300 m. Hydraulic fracturing of the two wells will be conducted to create parallel hydraulic fractures, and water will be circulated between these wells. Our modeling focuses on secondary, thermal fractures from the hydraulic fractures. In our modeling analyses, we use a reservoir temperature of 200°C, a confining stress of 32.2 MPa, and a fluid pressure of 22.5 MPa to represent the in situ conditions at the depth of interest. A fluid temperature of 50°C at the reservoir depth is used to represent a significant cooling of 150°C by fluid injection and circulation. The corresponding dimensionless effective confining stress is $\mathcal{T} = 0.1088$ for in situ fluid pressure.

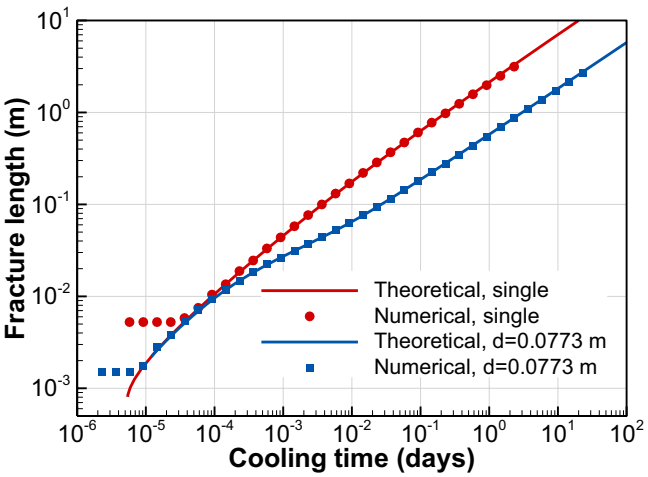

Figure 8. Comparison of the evolution of fracture length with cooling time between the theoretical and FEM solutions for single and constantly spaced thermal fractures.

4.2. Solution Validation

For the FEM analyses, rock deformation is governed by the linear elasticity theory and fracture propagation is governed by the LEFM. The stress intensity factor is computed according to the interaction energy integral method (Chen, Cen, et al., 2018; Menouillard & Belytschko, 2010). The thermal effects are represented by tractions along the surface of thermal fractures. A uniform stress equal to the effective confining stress, $\sigma_{ec} = 32.2 - 22.5 = 9.7$ MPa, toward the fractures is applied on the fracture surface to present an equivalent boundary condition. A sufficiently large model domain (10 m in width and 20 m in length) is used for the case of single thermal fracture (Case A) to approximate the infinite domain and discretized with 5,321,656 linear triangular elements. In the case of multiple fractures with constant spacing (Case B), a fracture spacing of $d = 0.0773$ m, which corresponds to a dimensionless fracture spacing of $\mathcal{D} = 100$, is used. Considering the symmetry of the problem, a half model domain with 0.0387 m in width and 20 m in length is used and discretized with 213,169 linear triangular elements. In the case of multiple fractures with dynamic spacing (Case C), a model domain with a width of 20 m and a length of 20 m is used and discretized with 2,127,997 linear triangular elements. An array of 200 initial fractures with a length of 0.1 m and an average spacing $d_0 = 0.1$ m is employed. (Note that the initial length only has an influence at the beginning of the simulation.) A perturbation $[-\Delta d, \Delta d]$ with $\Delta d = 0.1 d_0$ is randomly applied to the average fracture spacing (0.1 m) to have initial fractures with non-uniform spacing in range of $[d_0 - 2\Delta d, d_0 + 2\Delta d]$, as used in Tarasovs and Ghassemi (2014). For validation, the same mode-I fracture propagation is considered in the FEM modeling while the effect of fracture curvature is discussed in Section 5.2. A sufficiently small, dynamic time step is used to ensure that a few fractures propagate in each time step to accurately model fracture arrest.

For the theoretical solutions, the site-specific dimensionless effective confining stress $\mathcal{T} = 0.1088$ is used to calculate the dimensionless fracture length, spacing, and surface aperture in the three cases. The same initial fracture length and spacing (0.1 m) are used to start the fully transient solution in Case C. These dimensionless solutions are converted to their dimensional values using the site-specific parameters for comparison.

Figure 8 shows excellent agreement of fracture propagation for Cases A and B between the theoretical and FEM results. The fracture length calculated is 0.0116, 0.0497, 0.1906, 0.6772, 2.2899, and 7.5225 m in Case A and 0.0103, 0.0287, 0.0685, 0.2000, 0.6210, and 1.958 m in Case B at 10, 10^2, 10^3, 10^4, 10^5, and 10^6 s, respectively. The profile of fracture length in Case B deviates from that in Case A at around 10 s, and their late-time separation is by a factor of 3.840. The difference of time-dependent fracture length between Cases A and B shows the effect on fracture propagation of strong stress interaction between multiple closely spaced fractures. A similar agreement is achieved for Case B with different fracture spacing (not shown).

Figure 9 shows the fracture patterns predicted by the fully transient, theoretical solution and the FEM-based fracture model for Case C. Good agreement between the two solutions is achieved. First, the initial fractures start to propagate at a half hour in both solutions. The maximum length of propagating fractures by the theoretical and FEM solutions is 9.20 and 8.86 m at 150 days, respectively. Second, the overall fracture patterns between the two solutions are similar in terms of the number of propagating fractures and arrested fractures at different times (see Figure 10a for more quantitative comparison). Finally, the times of arrests are also similar between the two solutions. The main difference is between the sharp transitions from stable propagation to unstable arrest in the theoretical solution and the wider transitions between different arrested fractures in the FEM solution. These wide transitions are caused by the initial fractures with non-uniform spacing and the absence of the restriction on uniform spacing used in the theoretical solution.

To conduct a more quantitative validation, we calculate the average fracture spacing for different distance from the cooling surface from Figure 9b and compare it with three theoretical spacing solutions (i.e., the stepwise spacing with sharp transitions at fracture arrests from the initial spacing of 0.1 m and the continuous central line and arrest line of fracture spacing). As shown in Figure 10a, good agreement between the average fracture spacing

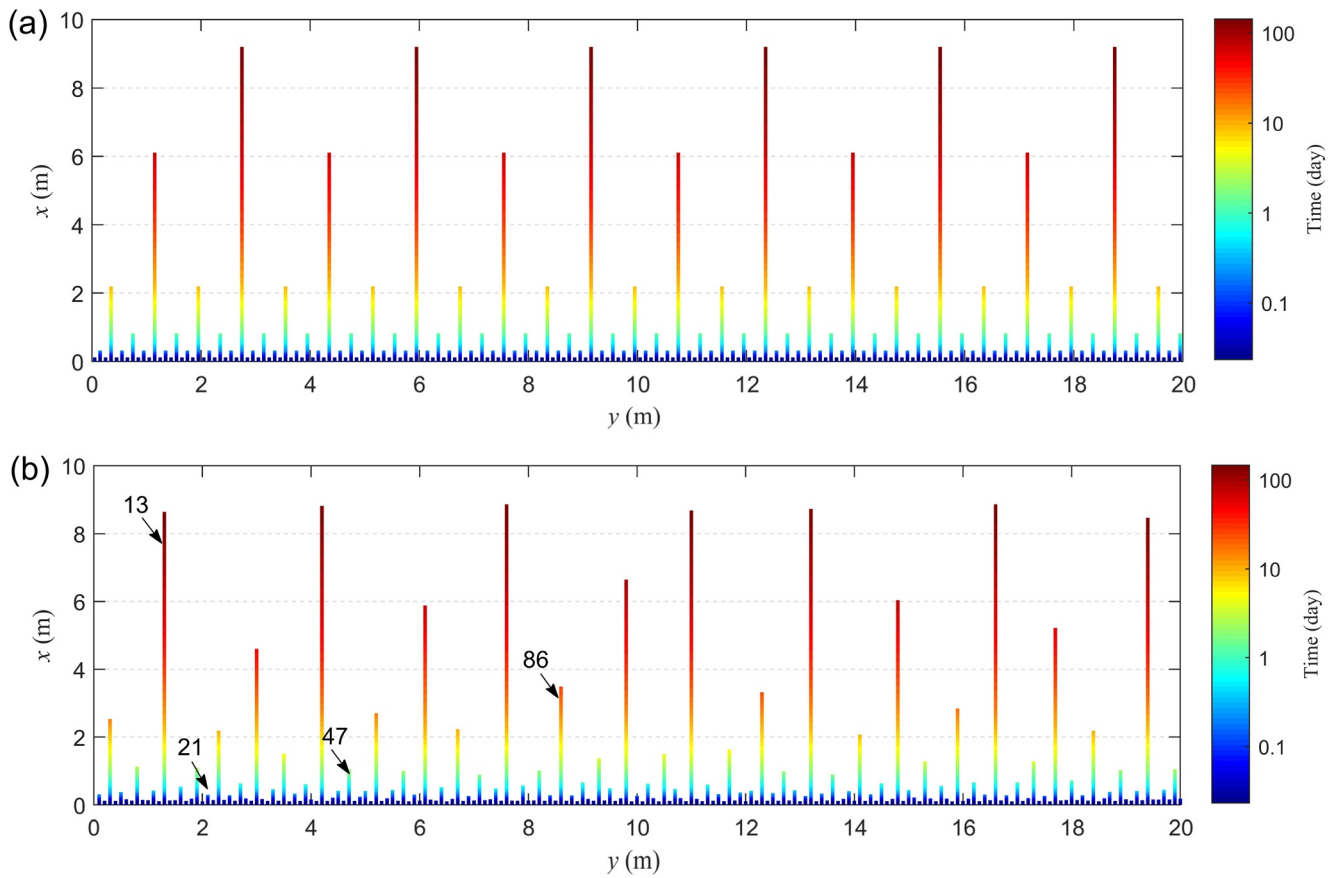

Figure 9. Comparison of propagation of thermal fractures for 150 days between (a) the fully transient theoretical solution and (b) the FEM solution. Each fracture is colored by cooling time (days) to show the dynamic evolution of fracture length and the arrest time can be seen at the tip of arrested fractures. The features of four selected individual fractures (#13, #21, #47, and #86) are shown in Figure 10.

in the FEM solution and the uniform fracture spacing in the theoretical central-line solution is observed, while a slight deviation of the FEM solution is likely caused by the randomness of initial and dynamic fracture spacing. The central-line solution is more appropriate than the stepwise solution to represent numerical solutions with non-uniform initial fracture spacing.

In addition, we select four individual fractures (#13, #21, #47, and #86 marked in Figure 9b) and compare the evolution of their length and surface aperture with the theoretical solutions (central and arrest lines) of propagating fractures. As shown in Figure 10b, each selected fracture propagates by exactly following the theoretical profile (the arrest line) until it is arrested, after which fracture length remains unchanged with time. The excellent agreement indicates that the theoretical solution can accurately predict the length of individual fractures during their propagation. The propagating fractures reach 0.14, 0.67, 6.25, and 78.00 m in 1 hr, 1 day, 100 days, and 10,000 days. (The result for 10,000 days is obtained by extending the profile based on the scaling law.) The corresponding theoretical fracture spacings are 0.16, 0.49, 2.30, and 13.00 m. This indicates that the length-to-spacing ratio is close to 1 at early time, increases to around 6 at 10,000 days, and keeps increasing for longer-term propagation.

As shown in Figure 10c, good agreement of the surface aperture (at the cooling surface) during fracture propagation is achieved between the theoretical and FEM solutions. The FEM surface aperture of the four selected fractures evolves by following the theoretical solution (the arrest line) until their arrest, after which their surface aperture (#21, #47, and #86) keeps decreasing significantly with time. Such a significant difference in fracture aperture between propagating and arrested fractures may be measurable in the field and used as an indicator of fracture state (propagating vs. arrested). The theoretical surface aperture of propagating fractures reaches 0.12,

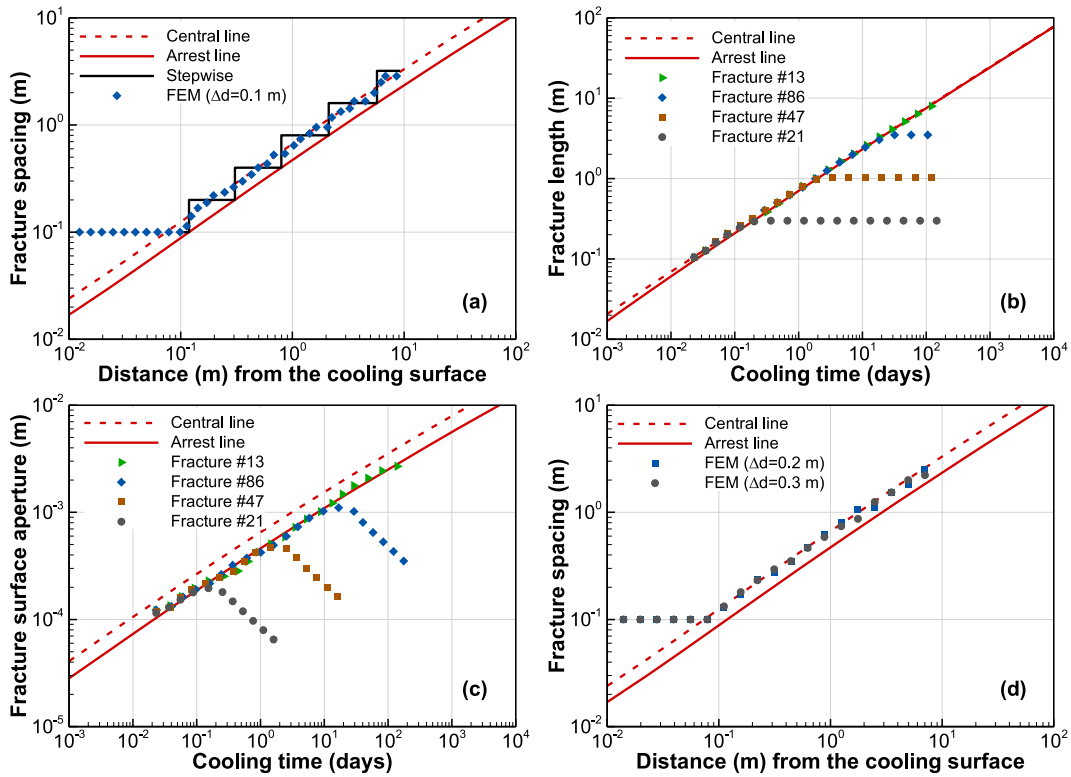

Figure 10. (a) Comparison between the uniform fracture spacing by the theoretical solution (stepwise, arrest, and central lines) and the average spacing by the FEM solution, comparison of (b) fracture length and (c) surface aperture between the theoretical solutions of propagating fractures and the FEM solutions of four selected fractures, and (d) spacing comparison for two FEM cases with different degrees of initial spacing nonuniformity.

0.43, 2.09, and 12.19 mm at 1 hr, 1 day, 100 days, and 10,000 days. The result for 10,000 days is obtained by extending the arrest line based on the scaling law.

The above validation for dynamically spaced fractures can be summarized: (a) the central-line theoretical solution can accurately predict the evolution of dynamic fracture spacing, (b) the arrest-line solutions can accurately predict the evolution of fracture length and surface aperture (as well as aperture profile along thermal fractures) for propagating fractures, and (c) the fully transient solution can predict the time-dependent pattern of propagating and arrested thermal fractures. When fracture pattern is not of interest, the profiles of central-line spacing and arrest-line length and surface aperture (prepared for different values of dimensionless effective confining stress) can be used directly for fast prediction.

4.3. Solution Applications

For the in situ fluid pressure at the Utah FORGE site used above, the fracture length, spacing, and surface aperture at 150 days of cooling predicted by our theoretical solutions are 9.2, 3.1, and 4.0 mm, respectively. These values are significant to field applications. When multiple parallel hydraulic fractures are created in a cluster of a stage during multistage hydraulic stimulation, the secondary thermal fractures initiated from neighboring hydraulic fractures are likely connected in the cooling zone to form a well-connected fracture zone for this cluster. With time, the multiple fracture zones associated with a stimulation stage are connected by the secondary thermal fractures. This thus enhances fracture-matrix heat exchange area (Harlow & Pracht, 1972; Murphy, 1978) and changes the fluid circulation system during EGS operation.

In addition to the base case (see Section 4.2), two additional fluid pressures (27.0 and 32.2 MPa) are used to investigate thermal fracturing under elevated pressure induced by water circulation. The effective confining stresses are $\sigma_{ec} = 5.2$ and 0 MPa, respectively. The fracture length in both cases is obtained using our theoretical

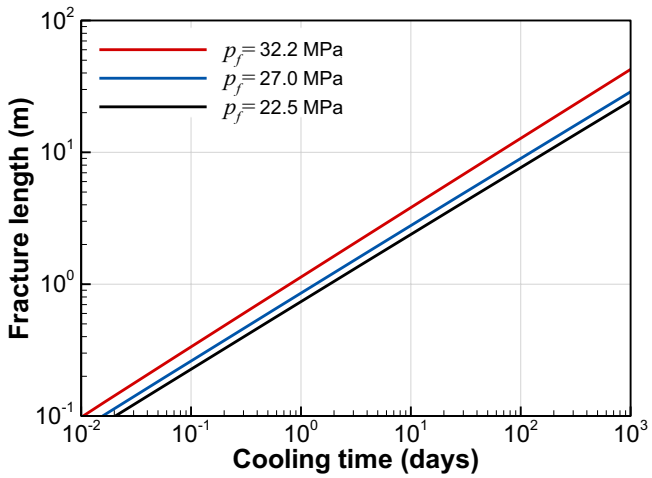

Figure 11. Evolution of fracture length under different fluid pressure in thermal fractures.

arrest-line solution with $\mathcal{T} = 0.0583$, 0.0 and compared with the base-case solution (Figure 11). Fractures propagate in a similar way under the same thermal stress in all the cases. The smaller the effective confining stress is, the longer fracture length is. The ratios of the fracture length, spacing, and surface aperture for $\sigma_{ec} = 9.7$, 5.2 and 0 MPa at 150 days are 1:1.18:1.74, 1:1.35:2.26, and 1:1.40:3.63. This means during EGS operation with pressure increase, the length, spacing, and surface aperture of thermal fractures can be as large as 16.0 m, 7.0 m, and 14.5 mm at 150 days for the highest fluid pressure at which the effective confining stress is exactly zero.

Note that for $\mathcal{T} = 0$, thermal stress is still needed for fractures to propagate because of the non-zero fracture toughness (see Table 1). For a pressure higher than 32.2 MPa, fracture propagation is no longer driven by thermal stress, and the fluid-driven propagation (i.e., hydraulic fracturing) is out of the scope of this study.

5. Discussion

The effects of several assumptions used in developing the theoretical solutions are discussed using additional FEM modeling and calculations, followed by how to use these solutions.

5.1. Effect of Non-Uniform Initial Fractures

The first assumption is the uniform spacing of thermal fractures, which helps solve the critical fracture length for a specific spacing and assemble the critical values into the dimensionless solutions, as used in previous studies (Bahr et al., 2010; Nemat-Nasser et al., 1978). In addition to perturbation $\Delta d = 0.1d_0$ in the base case, we add two additional cases with $\Delta d = 0.2d_0$ and $0.3d_0$ in the FEM-based simulation, while other parameters are kept unchanged from the base case. The results of average fracture spacing in the two cases (Figure 10d) are also in good agreement with the theoretical one in the base case. In addition, the fracture patterns in the three cases (not shown) are similar. All these comparisons indicate that the effect of non-uniform initial spacing is secondary to the effect of inter-fracture stress interaction and fracture arrest.

5.2. Effect of Fracture Curvature

The second assumption (that is also used in the above FEM modeling) is mode-I fractures without fracture curvature. To investigate this effect, we extend the FEM-based fracture model to account for mixed-mode fractures and thus fracture curvature. Three different cases with $\sigma_x = 24.4$, 32.2, and 40 MPa are used while σ_y is fixed at 32.2 MPa. The same values for rock properties and cooling conditions, as well as the randomly distributed initial fractures ($d_0 = 0.1$ m, $\Delta d = 0.1d_0$), as the base case are used. Mesh refinement is used to ensure that grid effects are negligible.

Figure 12 shows the simulated fracture patterns in the three cases with fracture curvature. The overall fracture curvature is the strongest in the case with the lowest σ_x (24.4 MPa), with a stress ratio of 1.32 higher than that (1.24) at the Utah FORGE site. Local fracture curvature of a propagating fracture occurs immediately after a neighboring fracture is arrested. Despite of local curvature, the overall trend for fractures to propagate in the direction perpendicular to the cooling surface is obvious. In addition, the fracture curvature tends to average fracture spacing and thus forms a hierarchical pattern instead of breaking it. For the other two cases, local fracture curving is nearly negligible. Moreover, the maximum length of propagating fractures at 150 days in the three cases is 9.10, 9.55, and 9.76 m, respectively, which are close to the theoretical value (9.20 m) in the same time period.

Figure 13 shows the comparisons of fracture spacing and length between the theoretical solution and the FEM solution for the case with the strongest curvature. More variations in the average fracture spacing are observed in Figure 13a than the mode-I results in Figure 10a. This is because fracture curvature leads to a more uniform fracture spacing and fracture arrests occur in a narrower distance window. Similar to the base case, the fracture

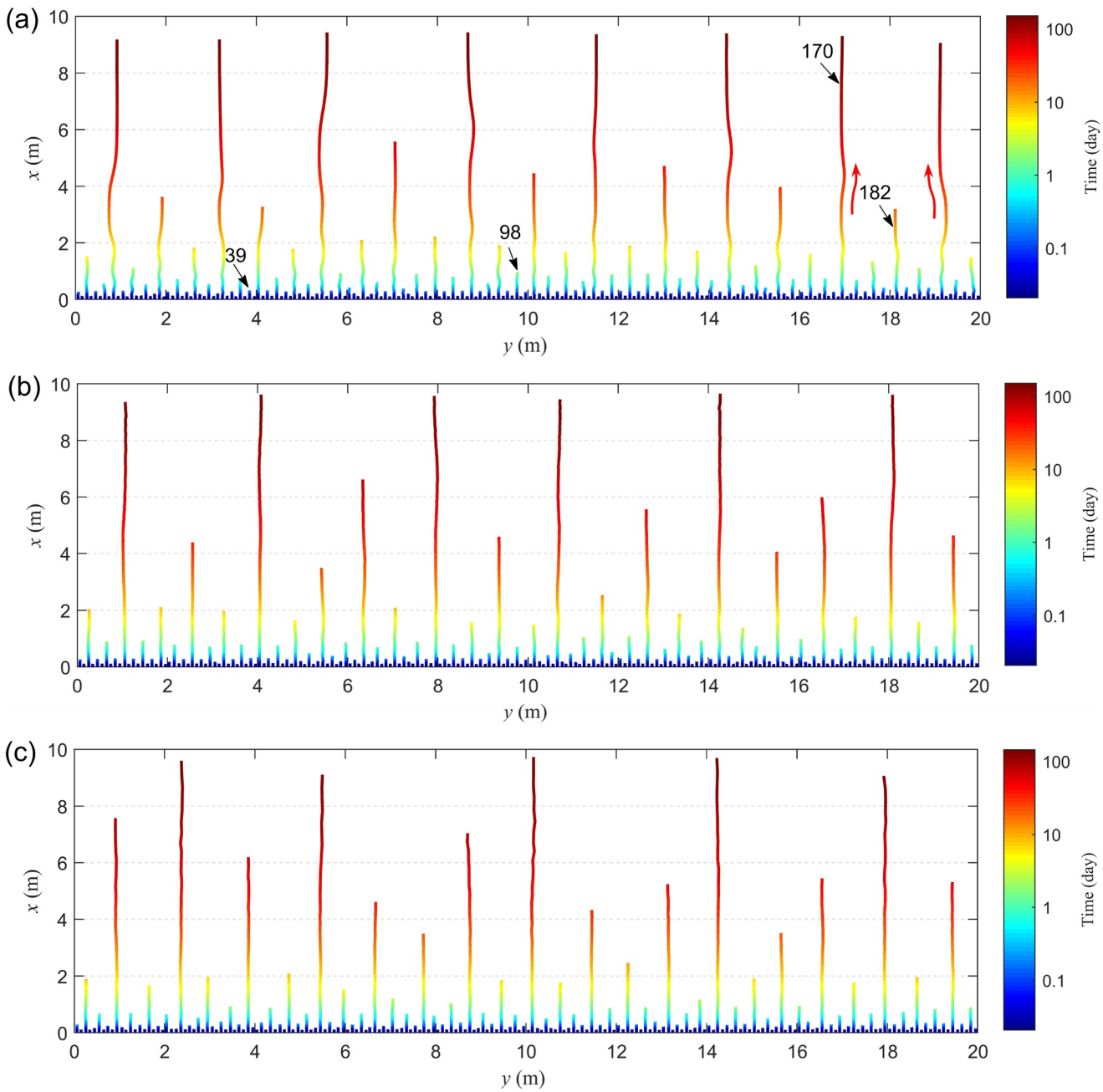

Figure 12. Transient fracture patterns with mixed-mode propagation of thermal fractures in 150 days under stress condition: (a) [24.4, 32.2] MPa, (b) [32.2, 32.2] MPa, and (c) [40, 32.2] MPa. Two red arrows in (a) show examples of fracture curvature induced by the arrest of a neighboring fracture. The features of four selected individual fractures (#39, #98, #170, and #182) are shown in Figure 13.

spacing still follows the central line, indicating that the theoretical solution of fracture spacing is valid for mixed-mode fractures. The length of propagating fractures is less affected by fracture curvature than fracture spacing and pattern, and an excellent agreement is obtained between the theoretical fracture length and the numerical length of four selected fractures during their propagation.

The effect of the no-curvature assumption is further investigated using the numerical solution in Tarasovs and Ghassemi (2011), in which mixed-mode fractures were modeled. The dimensionless effective confining stress $\mathcal{T}$ corresponding to the rock properties and cooling condition (for a confining stress of 20 MPa) given in Tarasovs and Ghassemi (2011) is 0.25. Our solutions of fracture spacing and length are converted from the dimensionless

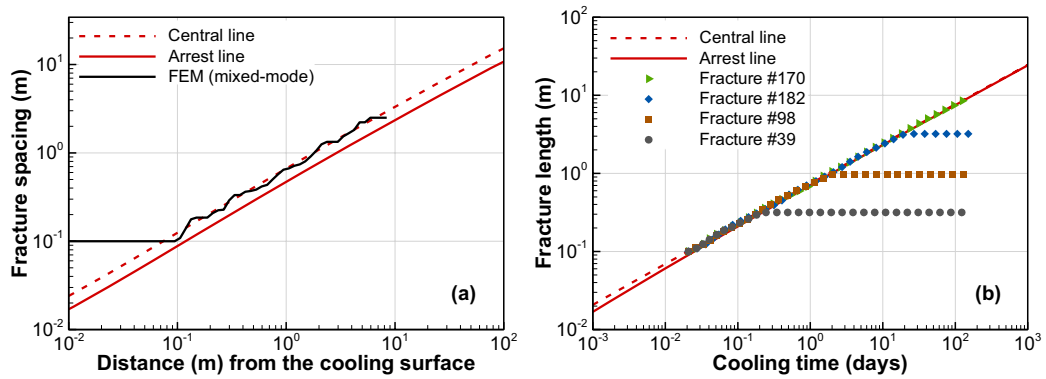

Figure 13. (a) Comparison between the uniform fracture spacing by the theoretical solution (arrest and central lines) and the average spacing by the FEM solution, and (b) comparison of fracture length between the theoretical solution and the FEM solutions for fractures #39, #98, #170 and #182 (marked in Figure 12a) in the case of mixed-mode fractures with $\sigma_x = 24.4$ MPa.

solutions for $\mathcal{T} = 0.25$. As shown in Figure 14, excellent agreements are observed for fracture spacing and length and their typical fracture pattern has characteristics similar to that shown in Figure 12.

In summary, mixed-mode fracture propagation has negligible effects on average spacing and length of propagating fractures, even though fracture curvature occurs under favorable stress conditions when neighboring fractures are arrested. Therefore, the effect of fracture curvature induced by non-uniform fracture spacing is believed to be secondary in forming a hierarchical fracture pattern. It is stress shadowing (i.e., inter-fracture stress interaction) that governs fracture arrest and thus the hierarchical fracture pattern. The stress shadowing is accurately accounted for in our theoretical solutions and its effect is clearly illustrated by comparing solutions of single fractures, and multiple constantly and dynamically spaced fractures.

5.3. Effect of Heat Convection

The third assumption is negligible heat convection in fractures and low-permeability reservoirs (compared to heat conduction through the rock matrix from the cooling surface). To investigate this effect, we quantitatively compare the total heat exchange through fracture surfaces and the cooling surface per unit width of the model in the y direction (with a unit of J/m^2). By assuming the fluid flowing into the fractures neither leaks into the matrix nor flows back to the main fluid channel, the upper limit of the former (E_f) is calculated by assuming all the fluid in the fractures is cooled by ΔT_s and estimating the fracture volume by a half of the product of fracture length and surface aperture. The latter (E_c) is computed by integrating the conductive heat flux through the cooling surface with time (Carslaw & Jaeger, 1959). The ratio of the two is expressed by

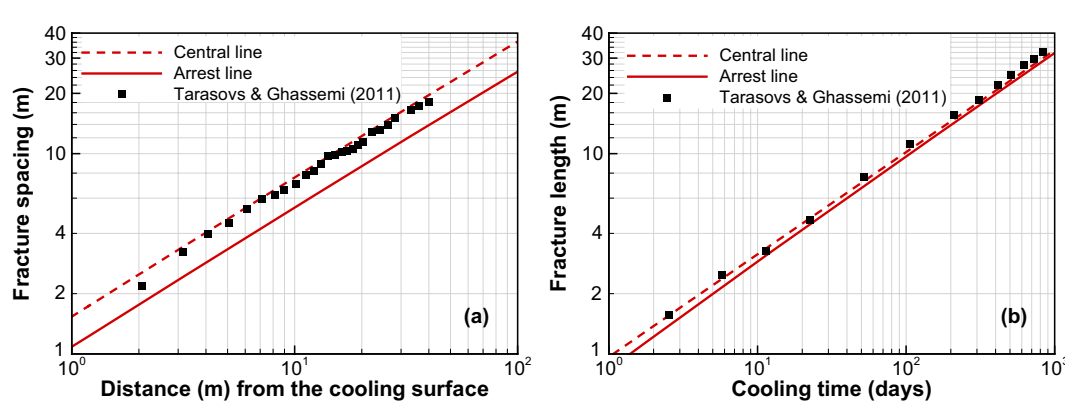

Figure 14. (a) Comparison between the uniform fracture spacing by the theoretical solution (arrest and central lines) and the average spacing by the numerical solution in Tarasovs and Ghassemi (2011), and (b) comparison of fracture length between the two solutions.

$$E_r = \frac{E_f(t)}{E_c(t)} = \frac{w_0(t)l(t)}{2d(t)}\Delta T_s \rho_w c_w / 2\lambda \Delta T_s \sqrt{\frac{t}{\pi D}} = \frac{\Omega_0(\tau)\mathcal{L}(\tau)}{4D(\tau)\sqrt{\tau}} \frac{\sqrt{\pi} D \rho_w c_w \beta \Delta T_s (1+\nu)}{\lambda} \tag{21}$$

where ρ_w and c_w are the density and specific heat capacity of the fluid, respectively, and w_0 is the surface aperture.

It can be proved that the first part of E_r, $\Omega_0(\tau)\mathcal{L}(\tau)/4D(\tau)\sqrt{\tau}$, is smaller than 1 over a reasonable range of time for a finite $\mathcal{T}$. The second part has a typical order of magnitude of $O(10^{-3})$ considering water properties, boundary conditions, and rock properties in Table 1. The calculated E_r of ~0.1% indicates that the heat exchange through thermal fractures is negligible for impervious reservoirs compared to heat conduction through the rock matrix from the cooling surface. In addition, the heat convection induced by the fluid flow from the cooling surface is usually assumed to have a negligible effect on the temperature distribution for a low-permeability rock, as shown by the numerical simulation for a rock permeability from 10^{-17} to 10^{-22} m^2 (Salimzadeh, Nick, et al., 2018).

When rock permeability is moderate or high, leakoff induced by injection-induced pressure increase ($p_f > p_0$) occurs from the thermal fractures (and the cooling surface) to the rock matrix, leading to non-negligible convective heat transfer in the fractures and rock matrix. This is the fourth scenario of thermal fracturing driven by heat conduction and convection (see Section 1.5), and numerical modeling is needed to capture the fully coupled THM-fracturing processes.

Recently, the coupled THM-fracturing processes have been simulated numerically for large-scale single and multiple vertical natural fracture(s) embedded in formations under thermal gradient (Patterson & Driesner, 2021; Stefansson et al., 2021). Initially, there is no water flow under hydrostatic pressure that corresponds to variable water density with in situ temperature variation in the vertical direction. The variable water density triggers convective flow within the fractures that develops, with upflow of lighter, warmer water, and downflow of cold water. The cold water flow cools the rock near the fractures, leading to high thermal stress and downward fracture growth. The coupled processes of natural convection and thermal fracturing may take a long time, depending on the magnitude of thermal gradient and the aperture, thickness, and spacing of the natural fractures (Patterson & Driesner, 2021). For a subsurface engineering application, the buoyancy effect and injection-induced forced convection may have different impacts on half-plane thermal fractures of interest in this study and need to be simulated numerically.

5.4. Effect of Rock Heterogeneities, Joints, and Natural Fractures

Rock is generally not a homogeneous material as assumed in our theoretical and numerical models. Rock heterogeneities, joints, and natural fractures may lead to the curvature of thermal fractures at different scales and induce fracture arrest. Thermal fractures likely initiate at these macroscale discontinuities or microscale inter-grain boundaries (e.g., Browning et al., 2016), and propagate along them when these discontinuities approximately align with the direction of thermal diffusion. A thermal fracture may be arrested when it intersects with such a discontinuity. When the approaching angle is small and the interaction from neighboring fractures is small, thermal stress is sufficient to reactivate the discontinuity, leading to a local fracture curvature. Other discontinuities between thermal fractures may have a minimum impact on the stress field and thus do not directly influence thermal fracturing. Once the length and spacing of thermal fractures become significantly larger than the size of these discontinuities, fracture propagation and arrest are mainly controlled by the macroscale stress distribution, while fracture arrest and local curvature induced by these discontinuities are secondary. Therefore, it is expected that discontinuities may affect the early propagation and arrest of thermal fractures but may not significantly alter the hierarchical fracture pattern shown in Figures 9 and 12 during long-term cooling. This is true for hot dry rock for EGS or unconventional shale with only microcracks (Murphy, 1978). In contrast, the pattern of thermal fractures may be significantly influenced by the well-connected network of dense natural fractures in hydrothermal fields. Further numerical studies are needed to give a guidance on when these discontinuities need to be considered in modeling thermal fracturing, like in the case of hydraulic fracturing (Chen et al., 2020; Gudmundsson, 2011).

5.5. Use of the Theoretical Solutions

The dimensionless solutions of dynamically spaced thermal fractures can be used for fast prediction of fracture properties (i.e., length, spacing, and surface aperture) for the entire spectrum of reservoir properties, in situ conditions, and circulation and cooling conditions. These solutions, with one model parameter ($\mathcal{T}$), present the transient profiles (referred to as type curves) of dimensionless fracture properties for a number of $\mathcal{T}$ (see Figure 7). (Type curves have been often used to represent analytical solutions of groundwater flow with one or two dimensionless parameters (Gringarten, 1984; Hantush, 1960).) As shown in the validation, the central-line solution of dimensionless spacing and the arrest-line solutions of dimensionless length and surface aperture for different $\mathcal{T}$ can be used to accurately approximate their fully transient solutions (see Figures 7 and 10). A solution table or contour for uniform increments of logarithm dimensionless time and effective confining stress can be created for each fracture property. For a site-specific application, the dimensionless solution of each fracture property can be obtained through interpolation of the corresponding table using the site-specific $\mathcal{T}$, leading to a single transient profile as shown in Figure 10. In addition, for long-term prediction, extrapolation can be performed based on the scaling law, with the scaling coefficient determined by fitting the late-time profile. In these cases, no computer runs are needed. Only when the fully transient solutions with stepwise fracture spacing are of interest for a specific initial fracture spacing, does the developed algorithm in Appendix C2 need to be run. Note that the dimensionless solution of single fracture and constantly spaced fractures cannot be used for predicting fracture properties of a site-specific application because they cannot capture the actual hierarchical fracture pattern.

No reactivation of arrested fractures in subsurface applications is found in this study and fracture reactivation is thus not considered. Chen and Zhou (2021) found that fracture reactivation is possible under no confining conditions, and affects fracture spacing and pattern; they considered fracture reactivation (in addition to fracture propagation and arrest) in their modeling. In that study, no model parameter is involved in dimensionless solutions (i.e., $\mathcal{T} = 0$) and the solution of fracture length is simply a single profile or type curve.

6. Summary and Conclusions

Cooling-induced thermal fracturing has been observed in many field applications associated with fluid injection and circulation in deep subsurface reservoirs. Critical to the accurate modeling of thermal fracturing is the fundamental understanding of (a) the temperature plume and thermal stresses that are the driving force of thermal fracturing, (b) stress interaction between multiple thermal fractures, and (c) fracture propagation and arrest. In this study, we consider the thermal fracturing of a confined two-dimensional half-plane, bounded by a hydraulic fracture (or other fluid channel) that is cooled by circulating (or flowing) fluid, using a plane strain model. The propagation and arrest of multiple dynamically spaced fractures are investigated using the stability analysis, with stress interaction computed using the DDM technique. Two simpler cases: propagation of multiple fractures with constant spacing (no fracture arrest) and of single fracture (i.e., with infinite spacing) are considered to better understand the mechanisms of fracture arrest and stress interaction. For the three cases, dimensionless transient solutions and late-time scaling laws are obtained from the dimensionless governing equations derived in terms of dimensionless fracture length $\mathcal{L}$, spacing $\mathcal{D}$, and aperture Ω, as well as dimensionless time τ and effective confining stress $\mathcal{T}$. The solutions of single fracture and dynamically spaced multiple fractures depend solely on one model parameter, $\mathcal{T}$.

For single fracture, the analytical solution is developed based on (a) directly calculating thermal stress using the analytical solution of one-dimensional heat conduction and (b) calculating the stress intensity factor and comparing it with rock toughness based on the LEFM theory. The solution shows that for a given dimensionless effective confining stress $\mathcal{T}$, dimensionless fracture length $\mathcal{L}$ starts from a critical initial length, increases nonlinearly with square root of dimensionless time $\left(\sqrt{\tau}\right)$, and then transitions to the scaling law of $\mathcal{L} = f(\mathcal{T})\sqrt{\tau}$ for late-time propagation. The scaling coefficient $f(\mathcal{T})$ decreases monotonically from $4/\left(\pi^{3/2}\mathcal{T}\right)$ for $\mathcal{T} \to 0$ to $\pi^{3/2}(1-\mathcal{T})/2$ for $\mathcal{T} \to 1$, showing the effect of dimensionless effective confining stress. The scaling law shows that late-time fracture length increases linearly with the square root of cooling time.

For constantly spaced multiple thermal fractures, the coupled elastic equilibrium equation and the fracture-propagation criterion are solved iteratively for dimensionless fracture length, $\mathcal{L}(\tau, \mathcal{D})$, and the profile of dimensionless fracture aperture. For a given $\mathcal{T}$, the $\mathcal{L}(\tau, \mathcal{D})$ solution deviates from the single-fracture solution $\mathcal{L}(\tau)$ at

a later τ for a higher spacing $\mathcal{D}$. After the deviation time, $\mathcal{L}(\tau, \mathcal{D}) < \mathcal{L}(\tau)$, indicating that the stress interaction between fractures slows down fracture propagation. The smaller $\mathcal{D}$ is, the stronger the stress interaction becomes, and the smaller $\mathcal{L}(\tau, \mathcal{D})$ is. A similar scaling law of $\mathcal{L} = f(\mathcal{D}, \mathcal{T})\sqrt{\tau}$, with scaling coefficient $f(\mathcal{D}, \mathcal{T})$ tabled for $(\mathcal{D}, \mathcal{T})$ pairs, is observed for late-time propagation, showing that the effects of effective confining stress and fracture spacing are separated from the effect of cooling time.

For dynamically spaced multiple fractures, their propagation is considered as a combination of a series of stable propagation (with constant fracture spacing) and unstable arrest (with spacing doubled at fracture arrest) that is determined by the stability analysis. The dimensionless solutions of fracture length, spacing, and aperture at the critical states of fracture arrests (i.e., arrest lines) for different $\mathcal{T}$ are obtained. The following features of the solutions are observed: (a) dimensionless dynamic fracture spacing increases with dimensionless time, with a small effect of $\mathcal{T}$, (b) both dimensionless fracture length and surface aperture increase with dimensionless time, with a stronger effect of $\mathcal{T}$, (c) the ratio of $\mathcal{L}$ to $\mathcal{D}$ is around 1 at small τ and increases with τ, and (4) the scaling law $\mathcal{L} = f'(\mathcal{T})\sqrt{\tau}$ is valid at late time. (The coefficient $f'(\mathcal{T})$ is smaller than $f(\mathcal{T})$ for single fracture.) Finally, the fully transient solutions of fracture properties are obtained by time-stepping of fracture propagation and arrest with stepwise fracture spacing.

The three analytical/dimensionless solutions are validated using a FEM-based fracture model (with mode-I fractures) for the settings of a real geothermal site. Excellent agreements are achieved for the evolution of fracture length for single fracture and constantly spaced multiple fractures. For dynamically spaced fractures, excellent agreements are also achieved for the evolution of fracture length, average spacing, and surface aperture, as well as fracture patterns, at all times. This validation shows that the developed dimensionless solutions can be used to rapidly predict the propagation of interacting thermal fractures under practical geological and engineering conditions at real geological sites (without time-consuming model construction and computation in general numerical modeling). The scaling law can be used to estimate long-term fracture properties. The applications to the Utah FORGE site for both in situ and elevated fluid pressures indicate that tens-meter long thermal fractures are created. These transverse thermal fractures can link parallel hydraulic fractures, created in multistage hydraulic stimulation, to form well-connected fracture zones in the cooling region, and thus enhance fracture-matrix heat exchange area and impact water circulation during EGS operation.

The theoretical solutions are reliable under certain conditions, such as low-permeability, low-porosity crystalline rock, or low-permeability unconventional shale. The two key assumptions of (a) uniform fracture spacing and (b) mode-I fractures used in developing the solutions have negligible effects on the solutions, as demonstrated by additional FEM modeling with non-uniformly distributed fractures and mixed-mode fracture propagation. Fracture curvature may occur under favorable stress conditions when neighboring fractures are arrested but has negligible effects on the *average* fracture spacing and length of propagating fractures. It is stress shadowing that governs fracture arrest and thus the hierarchical fracture pattern. The stress shadowing (i.e., inter-fracture stress interaction) is accurately accounted for in our theoretical solutions using the DDM and its effect is clearly illustrated by comparing solutions of single fractures, and multiple constantly and dynamically spaced fractures. The influences of heat convection, rock heterogeneities, joints, and natural fracture are also discussed.

Appendix A: Solution Approach for Single Thermal Fracture

A1. Analytical Transient Solution for Single Fracture

The propagation of single thermal fracture is governed by Equation 12, with one model parameter, dimensionless effective confining stress $\mathcal{T}$. The analytical, transient solution of dimensionless fracture length is derived. Equation 12 is inspected and found to have a complicated integral. For better discussion, we use $\mathcal{F}(\mathcal{L}, \tau, \mathcal{T})$ to denote the left-hand side of Equation 12. We calculate $\mathcal{F}$ as a function of $\mathcal{L}$ at different τ. Figure A1a shows the profiles of $\mathcal{F}$ at different τ for $\mathcal{T} = 0.5$. Each profile has an ascending limb and a descending limb and fracture propagation occurs when $\mathcal{F} > 1$. There exists a critical dimensionless time τ_c that ensures the existence of the solution for $\mathcal{F} = 1$. For $\mathcal{T} = 0.5$ and $\tau_c = 10^{1.56}$, the corresponding solution for $\mathcal{F} = 1$ is $\mathcal{L}_c = 2.99$. For $\tau > \tau_c$, two solutions of $\mathcal{L}$ are obtained. The smaller one is the minimum length required for the initial fracture to be activated at current τ. The larger one represents the length of the stably propagating fracture. Evolution of the two solutions for $\mathcal{T} = 0.5$ is shown in Figure A1b.

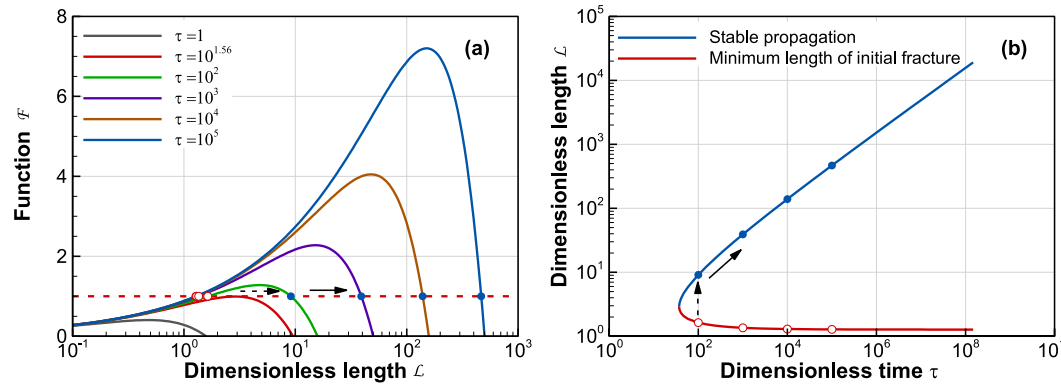

Figure A1. Propagation of single thermal fracture for $\mathcal{T} = 0.5$. (a) Profiles of function $\mathcal{F}(\mathcal{L}, \tau, \mathcal{T})$ (solid lines) and the actual solutions of dimensionless fracture length in the descending limbs (blue solid circles) with $\mathcal{F} = 1$ (dashed line) at different times, as well as the solutions in the ascending limbs (red hollow circles). The solid arrow represents stable propagation while the dashed arrow indicates unstable fracture propagation. (b) Length of stably propagating fracture and the minimum length of initial fracture (as a function of dimensionless time τ).

The initial fracture with a length $\mathcal{L}_{int} \geq \mathcal{L}_c$ or $\mathcal{L}_{int} < \mathcal{L}_c$ has different behavior after initiation. For the former, the fracture is activated at some time and starts to propagate in a stable mode. For example, with $\mathcal{L}_{int} = 9.12$ at the leftmost solid circle in Figures A1a and A1b, the fracture starts to propagate at $\tau = 100$ and the fracture length increases gradually with time. With $\mathcal{L}_{int} \leq \mathcal{L}_c$ (e.g., $\mathcal{L}_{int} = 1.63$ at the rightmost hollow circle in Figure A1a or the leftmost hollow circle in Figure A1b), the fracture also starts to propagate at $\tau = 100$ but instantaneously reaches to $\mathcal{L} = 9.12$ in an unstable mode since $\mathcal{F} > 1$ is always satisfied in the range $1.63 < \mathcal{L} < 9.12$ at $\tau = 100$ and continues to propagate in a stable mode (see Figure A1b). The similar unstable behavior of single thermal fracture free of confining stress has been discussed in the literature (Bahr et al., 1993; B. Wang et al., 2015). In this study, we focus on the stable fracture propagation by specifying a reasonable initial fracture length equal to or larger than the critical fracture length. The instant initiation of thermal fractures in intact rock is beyond the scope of this study.

A2. Derivation of Scaling Law for Late-Time Propagation of Single Fracture

For late-time fracture propagation under finite effective confining stress (i.e., $\mathcal{T} > 0$, $\tau \to \infty$ and $\mathcal{L} \to \infty$), the dimensionless governing equation for single thermal fracture, Equation 12, degrades to

$$\int_0^1 \frac{1}{\sqrt{1-\xi^2}} \operatorname{erfc}\left(\frac{\mathcal{L}}{2\sqrt{\tau}}\xi\right) \mathrm{d}\xi = \frac{\pi}{2}\mathcal{T} \tag{A1}$$

The left-hand side term of Equation A1 has a maximum value of $\pi/2$. For an arbitrary $0 < \mathcal{T} < 1$, $\mathcal{L}/\sqrt{\tau}$ is a constant and can be solved from Equation A1.

For $\mathcal{T}$ close to 1, we use the Taylor expansion for $\operatorname{erfc}(\omega)$ at $\omega = 0$ and obtain

$$\int_0^1 \frac{1}{\sqrt{1-\xi^2}} \operatorname{erfc}\left(\frac{\mathcal{L}}{2\sqrt{\tau}}\xi\right) d\xi \approx \int_0^1 \frac{1}{\sqrt{1-\xi^2}} \left(1 - \frac{1}{\sqrt{\pi}}\frac{\mathcal{L}}{\sqrt{\tau}}\xi\right) d\xi = \frac{\pi}{2} - \frac{1}{\sqrt{\pi}}\frac{\mathcal{L}}{\sqrt{\tau}} \tag{A2}$$

Combining Equations A1 and A2, we have

$$\frac{\mathcal{L}}{\sqrt{\tau}} = \frac{\pi^{3/2}}{2}(1-\mathcal{T}) \tag{A3}$$

For $\mathcal{T}$ close to zero, $\mathcal{L}/\sqrt{\tau}$ approaches to infinity according to Equation A1. The left-hand-side term of Equation A1 can be rewritten:

$$\int_0^1 \frac{1}{\sqrt{1-\xi^2}} \operatorname{erfc}\left(\frac{\mathcal{L}}{2\sqrt{\tau}}\xi\right) d\xi = \int_0^1 \operatorname{erfc}\left(\frac{\mathcal{L}}{2\sqrt{\tau}}\xi\right) d\xi + \int_0^1 \left(\frac{1}{\sqrt{1-\xi^2}} - 1\right) \operatorname{erfc}\left(\frac{\mathcal{L}}{2\sqrt{\tau}}\xi\right) d\xi \tag{A4}$$

The infinite $\mathcal{L}/(2\sqrt{\tau})$ leads to a very small range of ξ, out of which erfc $\left(\frac{\mathcal{L}}{2\sqrt{\tau}}\xi\right)$ is essentially zero. The second term in Equation A4 is thus negligible, and we have

$$\int_0^1 \frac{1}{\sqrt{1-\xi^2}}\text{erfc}\left(\frac{\mathcal{L}}{2\sqrt{\tau}}\xi\right)d\xi \approx \int_0^1 \text{erfc}\left(\frac{\mathcal{L}}{2\sqrt{\tau}}\xi\right)d\xi = \frac{2\sqrt{\tau}}{\mathcal{L}}\int_0^{\frac{\mathcal{L}}{2\sqrt{\tau}}} \text{erfc}(\omega)d\omega = \frac{2\sqrt{\tau}}{\mathcal{L}\sqrt{\pi}} \tag{A5}$$

From Equation A1, we have

$$\frac{\mathcal{L}}{\sqrt{\tau}} = \frac{4}{\pi^{3/2}\mathcal{T}} \tag{A6}$$

Appendix B: Solution Approach for Constantly Spaced Thermal Fractures

For propagation of an infinite number of parallel thermal fractures with constant spacing, we use a large number $(2n+1)$ of fractures to approximate the infinite fracture condition (see Figure B1a), each of which has an actual fracture at $x \geq 0$ and an image fracture at $x \leq 0$ to form a symmetric problem along the cooling surface. (This boundary condition is used to simplify the hydraulic fracture or fluid channel with possible contraction in the x direction neglected. This simplification only affects the early time solution of fracture length.) All the (actual) fractures have equal length and identical profiles of normal stress and dimensionless aperture. Each actual (or image) fracture is discretized into N_x displacement discontinuity (DD) elements of identical length, with element N_x closest to the fracture tip and element 1 next to the cooling surface. N_x needs to be sufficiently large to accurately capture the stress interaction between neighboring fractures. Both N_x and n are set to 500+ Round$(50\mathcal{L}/D)$, where Round() returns the rounded integer.

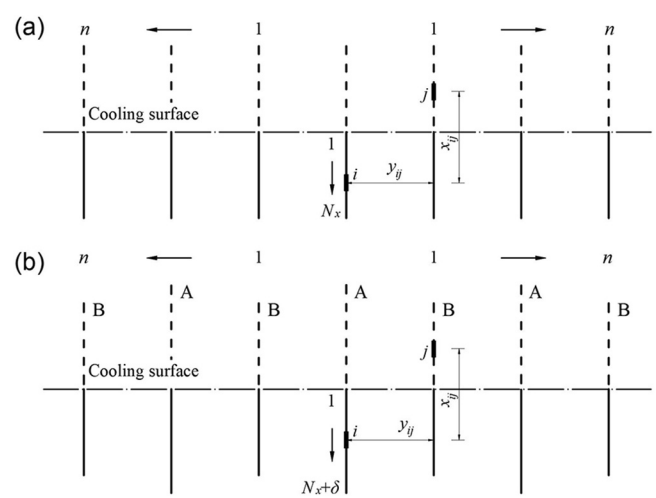

Figure B1. Diagram of DDM discretization of $(2n+1)$ parallel (actual and image) fractures, and contribution to the influence matrix from the stress interaction between element i in the center fracture and element j in the k' th ($k'=1$) fracture: (a) multiple fractures with equal length and (b) multiple fractures in subsets A and B with different length (reused from Chen and Zhou [2021]).

In the case of multiple thermal fractures with equal length, the discretization of Equation 15 using DDM leads to

$$\frac{1}{4\pi}\ \mathbf{M\Omega} = \mathbf{\Pi} \tag{B1}$$

where $\mathbf{M}$ is the dimensionless influence matrix that reflects the resultant effect of all the fractures on the center fracture, $\mathbf{\Omega}$ is the dimensionless aperture vector, and $\mathbf{\Pi}$ is the normal stress vector. More specifically, we have

$$\mathbf{M} = \mathbf{M}_0 + 2\sum_{k'=1}^{n}\mathbf{M}_{k'} \tag{B2a}$$

$$\mathbf{\Omega} = \left[\Omega_1,\ \Omega_2,\ \ldots\ ,\Omega_{2N_x}\right]^T \tag{B2b}$$

$$\mathbf{\Pi} = \left[\Pi_1,\ \Pi_2,\ \ldots\ ,\Pi_{2N_x}\right]^T \tag{B2c}$$

$$\Pi_i = \mathrm{erfc}\left(\frac{\mathcal{X}_i}{2\sqrt{\tau}}\right) - \mathcal{T} \tag{B2d}$$

where $\mathbf{M}_{k'}$ ($k' = 0,\ 1,\ 2,\ \ldots, n$) represents the influence of the k'th fracture located at $y = k'd$ on the center fracture and $\mathcal{X}_i$ is the dimensionless distance at the midpoint of element i. $\mathbf{M}_{k'}$ is given by the dimensionless influence matrix A_{ij} with element i on the center fracture and element j on the k' th fracture (see Appendix A in Chen and Zhou [2021]). Note that $\mathbf{M}$ is a function of $\mathcal{L}$ and $\mathcal{D}$ and $\mathbf{\Pi}$ is a function of $\mathcal{T}$ and τ.

Similarly, the dimensionless fracture-propagation criterion in Equation 16 can be rewritten:

$$\mathcal{L} = \frac{\pi C^2}{32\left(1 - \xi_{N_x}\right)}\Omega_{N_x}^2 \tag{B3}$$

where $\xi_{N_x} = \mathcal{X}_{N_x}/\mathcal{L}$, C is the coefficient used to correct the stress intensity factor computed with constant DD elements, and Ω_{N_x} is the fracture aperture of the N_x th DD element. $C = 0.798$ is used according to Mériaux and Lister (2002).

Equations B1 and B3 are coupled by two unknowns: $\mathcal{L}$ and $\mathbf{\Omega}$, and are solved iteratively in each time step (τ), for which the normal stress vector is known. $\mathbf{\Omega}$ is first obtained by solving Equation B1 with the $\mathcal{L}$ value in the last time step (an initial $\mathcal{L}_{ini}$ needs to be specified for the first time step). With Ω_{N_x} known, $\mathcal{L}$ is then updated using Equation B3. The iteration is repeated until the convergence of $\mathcal{L}$, and the solutions of $\mathcal{L}$ and $\mathbf{\Omega}$ are obtained. Then the program moves to the next time step. The time stepping is repeated from the initial time to a large τ to obtain the transient solution of dimensionless fracture length (as well as the aperture profile at each time). The iterative procedure with time stepping is the same as that often used in numerical simulators for coupled problems.

Appendix C: Solution Approach for Dynamically Spaced Thermal Fractures

The fracture propagation with dynamic spacing can be considered as a combination of a series of stable propagation (with constant spacing) and unstable arrest (with fracture spacing doubled at fracture arrest). Figure C1a shows the path of the change in dimensionless fracture spacing, as a function of dimensionless distance from the cooling surface ($\mathcal{X}$), for a given initial spacing $\mathcal{D}_0$, along with the lower and upper envelopes of the solution path. At the lower envelope (referred to as the arrest line), the instability condition of fracture arrest occurs, and propagating fractures can only propagate with some fractures arrested. The arrest line $\mathcal{D}_a$ ($\mathcal{X}_a$) is the separator between the stable state and the unstable state.

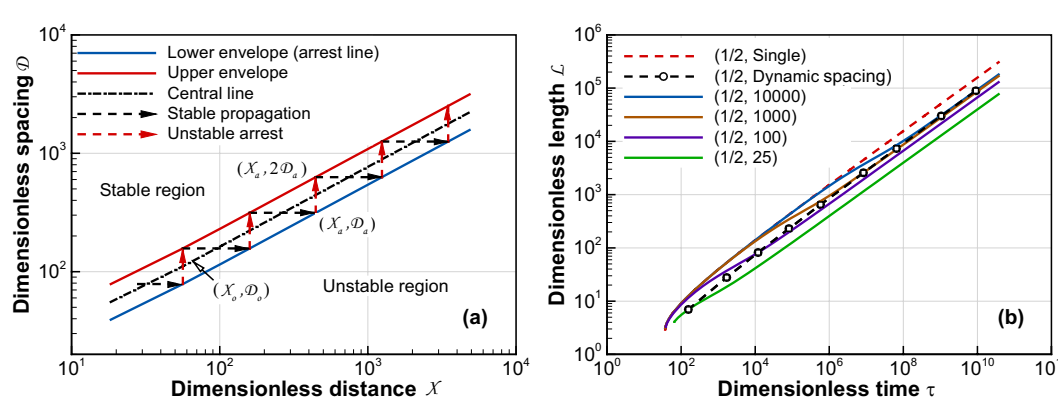

Figure C1. (a) A schematic fracture solution path consisting of stable propagation and unstable arrest of multiple fractures, bounded by the upper envelope and the lower envelope (i.e., the arrest line separating the stable and unstable regions), illustrated for $\mathcal{T} = 0.5$. The central line shows an approximate solution assuming a continuous fracture spacing. (b) Determination of the arrest line for $\mathcal{T} = 0.5$ by linking the critical states (hollow circles) for $\mathcal{D} = [25, 50, 100, 200, 400, 1000, 2000, 5000, 10000]$, along with the constant-spacing solutions for four $\mathcal{D}$ values and the single-fracture solution.

The procedure of solving for the properties of dynamically spaced thermal fractures includes: (a) determination of the critical states at fracture arrest (arrest lines) by calculating the critical dimensionless fracture length $\mathcal{L}_a(\mathcal{D}_i)$, time $\tau_a(\mathcal{D}_i)$, and aperture $\mathbf{\Omega_a}(\mathcal{D}_i)$ ($\mathbf{\Omega_a}$ is the vector of the discretized dimensionless aperture along the thermal fracture at the arrest line and has a length of $2N_x$) at the unstable condition using the stability analysis for a series of dimensionless spacing $\mathcal{D}_i$, (b) determination of the approximate solutions (central line), and (c) determination of fully transient solution of fracture properties with stepwise fracture spacing.

C1. Determination of the Arrest Lines and Approximate Solutions

The algorithm for determining the arrest lines is described in Figure C2. For a series of given spacing $\mathcal{D}_i$, we record $\tau_a(\mathcal{D}_i)$, $\mathcal{L}_a(\mathcal{D}_i)$, and $\mathbf{\Omega_a}(\mathcal{D}_i)$ and link them to form a continuous solution $(\tau_a, \mathcal{L}_a, \mathbf{\Omega}_a, \mathcal{D}_a)$ at the arrest lines. Figure C1 shows an example (black dashed line) of arrest line $\mathcal{L}_a(\mathcal{D}_i)$ by linking the hollow circles of nine different dimensionless fracture spacing in the case of $\mathcal{T} = 0.5$. With the arrest lines known, the fracture pattern after arrests for a specified initial spacing can be predicted by following the fracture path shown in Figure C1a. In this case, only the solutions at the arrest times are known, which are sufficient for most cases as shown in Section 4.2.

For the details of stability analysis, we divide the $2n+1$ fractures into subsets A and B alternately (see Figure B1b). Without loss of generality, we define subset A fractures as propagating fractures and subset B ones as fractures to be arrested, and artificially extend the former by $\sim 0.01\mathcal{L}$ (i.e., $\mathcal{L}_A \approx 1.01\mathcal{L}$, $\mathcal{L}_B = \mathcal{L}$). The subset B fractures are discretized by N_x DD elements and the subset A fractures are discretized by $N_x + \delta$ DD elements, with identical length for all elements. Note that the center fracture can be in subset A or B. The discretized form of Equation 15 for subset A with the center fracture (see Figure B1b) can be written

$$\frac{1}{4\pi}\left(\mathbf{M^{AA}\Omega^A} + \mathbf{M^{BA}\Omega^B}\right) = \mathbf{\Pi^A} \tag{C1}$$

The discretized form of Equation 15 for subset B with the center fracture can be written

$$\frac{1}{4\pi}\left(\mathbf{M^{AB}\Omega^A} + \mathbf{M^{BB}\Omega^B}\right) = \mathbf{\Pi^B} \tag{C2}$$

where $\left(\mathbf{\Omega^A}, \mathbf{\Pi^A}\right)$ and $(\mathbf{\Omega^B}, \mathbf{\Pi^B})$ are the vector pairs of the dimensionless fracture aperture and normal stress for subsets A and B, respectively. $\mathbf{M^{AA}}$, $\mathbf{M^{BA}}$, $\mathbf{M^{AB}}$, and $\mathbf{M^{BB}}$ are the influence matrices between subsets A and B. $\mathbf{M^{AA}}$ and $\mathbf{M^{BA}}$, reflecting the resultant effect of fractures in subsets A and B on the center fracture in subset A, are computed by

$$\mathbf{M^{AA}} = \mathbf{M}_0 + 2\sum_{k'\in[1,n]\ \ in\ \ subset\ \ \mathrm{A}} \mathbf{M}_{k'} \tag{C3a}$$

$$\mathbf{M^{BA}} = 2\sum_{k'\in[1,n]\ \ \mathrm{in}\ \ subset\ \ \mathrm{B}} \mathbf{M}_{k'} \tag{C3b}$$

Similarly, $\mathbf{M^{BB}}$ and $\mathbf{M^{AB}}$ that include the resultant effect of fractures in subsets A and B on the center fracture in subset B are computed.

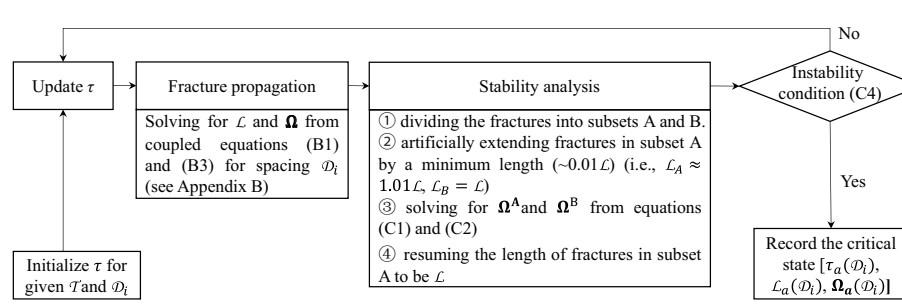

Figure C2. Algorithm for solving for critical fracture properties for a specific dimensionless confining stress and fracture spacing using the stability analysis.

With $\mathbf{\Omega^A}$ and $\mathbf{\Omega^B}$ solved from Equations C1 and C2, the discretized, equivalent dimensionless form of the instability condition in Equation 8 turns into

$$\Omega^A_{N_x+\delta} > \Omega^B_{N_x} \tag{C4}$$

where $\Omega^A_{N_x+\delta}$ and $\Omega^B_{N_x}$ are the fracture aperture of the $(N_x + \delta)$ th DD element in subset A fractures and the N_x th DD element in subset B fractures. Equation C4 is used to determine whether fracture arrest occurs during fracture propagation with time for a given fracture spacing.

The fracture path in Figure C1a can be approximately represented by the central line denoted by $(\tau_o, \mathcal{L}_o, \mathbf{\Omega}_o, \mathcal{D}_o)$ with $\mathcal{D}_o = \sqrt{2}\mathcal{D}_a$ and $\mathcal{L}_o = \mathcal{L}_a$. $\mathbf{\Omega}_o$ is the vector of the discretized dimensionless aperture along the thermal fracture at the central line and has a length of $2N_x$. τ_o and $\mathbf{\Omega}_o$ need to be solved from Equations B1 and B3 by setting $\mathcal{D}_o = \sqrt{2}\mathcal{D}_a$ and $\mathcal{L}_o = \mathcal{L}_a$. The solutions at the central line provide approximate solutions of multiple thermal fractures with dynamic spacing assuming a continuous change of fracture spacing. The results of the arrest lines of $(\tau_a, \mathcal{L}_a, \mathbf{\Omega}_a, \mathcal{D}_a)$ for different $\mathcal{T}$ are given in Section 3.2.3 while both the solutions at the arrest line and the central line are given in their dimensional manner in Section 4.2.

C2. Fully Transient Solutions of Fracture Properties

The solutions of the arrest line $(\tau_a, \mathcal{L}_a, \mathbf{\Omega}_a, \mathcal{D}_a)$ and the central line $(\tau_o, \mathcal{L}_o, \mathbf{\Omega}_o, \mathcal{D}_o)$ provide continuous solutions of fracture properties, which are sufficient to capture the evolution of fracture length, spacing, and aperture as shown in the solution validation and application in Section 4. In some rare cases, fully transient solutions of fracture properties with stepwise fracture spacing $(\mathcal{D}_0, 2\mathcal{D}_0, 4\mathcal{D}_0, \ldots)$ are of interest, in particular, for fracture pattern. These solutions can be solved through following steps. To start the modeling, we pick up an arbitrarily small fracture spacing $\mathcal{D}_0$ and a sufficiently large number of fractures (2^m). The initial fracture length $(\mathcal{L}_{int})$ is determined by satisfying $\mathcal{D}_a(\mathcal{L}_{int}) < \mathcal{D}_0$ to ensure the initial state $(\mathcal{L}_{int}, \mathcal{D}_0)$ is in the stable region above the arrest line (see Figure C1a). We then perform the fracture propagation by solving for $\mathcal{L}$ and $\mathbf{\Omega}$ from coupled Equations B1 and B3 until fracture length for current spacing reaches the arrest line. At the unstable arrest, every other propagating fracture (subset B fracture) is arrested and the rest of propagating fractures (subset A fractures) with a doubled spacing continue to propagate until the next arrest event. Note that the selection of subset A and B does not affect the fracture pattern because of the alternating nature of propagating and arrested fractures considered. This process is repeated until the final modeling time is reached. The fully transient solutions provide stepwise fracture spacing (Figures 10a and C1a), continuous fracture length, and fracture pattern (see Figure 9a) as functions of time. Note that as long as the arrest line is available, no stability analysis is further needed in the solution procedure.

Data Availability Statement

The modeling data of our developed analytical/dimensionless solutions and the computer code for obtaining these solutions are available on the website of Open Science Framework (https://osf.io/u3bcz/). No field or laboratory data are involved in this study.

Acknowledgments
The authors would like to thank Editor Douglas Schmitt and the Associate Editor, as well as Prof. Agust Gudmundsson at Royal Holloway, University of London, Egham, UK and other five anonymous reviewers, for their constructive comments and suggestions that help greatly improve the manuscript. This work was supported by the Assistant Secretary for Fossil Energy, National Energy Technology Laboratory, U.S. Department of Energy, under award DE-AC02-05CH11231 with Lawrence Berkeley National Laboratory (LBNL), through the project of National Risk Assessment Partnership (NRAP). Permission of Elsevier for re-using or modifying the figures in our previous study is acknowledged.

References

Adachi, J. I., & Detournay, E. (2002). Self-similar solution of a plane-strain fracture driven by a power-law fluid. *International Journal for Numerical and Analytical Methods in Geomechanics*, *26*(6), 579–604. https://doi.org/10.1002/nag.213

Adachi, J. I., & Detournay, E. (2008). Plane strain propagation of a hydraulic fracture in a permeable rock. *Engineering Fracture Mechanics*, *75*(16), 4666–4694. https://doi.org/10.1016/j.engfracmech.2008.04.006

Axelsson, G., Thórhallsson, S., & Björnsson, G. (2006). Stimulation of geothermal wells in basaltic rock in Iceland. Paper presented at the Enhanced Geothermal Innovative Network for Europe Workshop 3. Zürich.

Bahr, H.-A., Bahr, U., Gerbatsch, A., Pflugbeil, I., Vojta, A., & Weiss, H.-J. (1996). Fracture mechanical analysis of morphological transitions in thermal shock cracking. In R. D.Bradt (Ed.), *Fracture mechanics of ceramics* (pp. 507–522). Plenum Press.

Bahr, H.-A., Fett, T., Hahn, I., Munz, D., & Pflugbeil, I. (1993). Fracture mechanics treatment of thermal shock and the effect of bridging stresses. In G. A.Schneider, & G.Petzow (Eds.), *Thermal shock and thermal fatigue behavior of advanced ceramics* (pp. 105–117). Springer. https://doi.org/10.1007/978-94-015-8200-1_9

Bahr, H.-A., Fischer, G., & Weiss, H. J. (1986). Thermal-shock crack patterns explained by single and multiple crack propagation. *Journal of Materials Science*, *21*(8), 2716–2720. https://doi.org/10.1007/BF00551478

Bahr, H.-A., Weiss, H.-J., Bahr, U., Hofmann, M., Fischer, G., Lampenscherf, S., et al. (2010). Scaling behavior of thermal shock crack patterns and tunneling cracks driven by cooling or drying. *Journal of the Mechanics and Physics of Solids*, *58*(9), 1411–1421. https://doi.org/10.1016/j.jmps.2010.05.005

Barr, D. T. (1980). *Thermal cracking in nonporous geothermal reservoirs* (Master thesis). Massachusetts Institute of Technology.

Bažant, Z. P., Ohtsubo, H., & Aoh, K. (1979). Stability and post-critical growth of a system of cooling or shrinkage cracks. *International Journal of Fracture*, *15*(5), 443–456. https://doi.org/10.1007/BF00023331

Bradford, J., McLennan, J., Moore, J., Podgorney, R., Nash, G., Mann, M., et al. (2016). Numerical modeling of the stimulation program at RRG-9 ST1, a DOE EGS. Paper presented at the 41st Workshop on Geothermal Reservoir Engineering.

Bradford, J., Moore, J., Ohren, M., McLennan, J., Osborn, W. L., Majer, E., et al. (2015). Recent thermal and hydraulic stimulation results at Raft river, ID EGS Site. Paper presented at the 40th Workshop on Geothermal Reservoir Engineering.

Brown, D., Duchane, D., Heiken, G., & Hriscu, V. (2012). *Mining the Earth's heat: Hot dry rock geothermal energy*. Springer.

Browning, J., Meredith, P., & Gudmundsson, A. (2016). Cooling-dominated cracking in thermally stressed volcanic rocks. *Geophysical Research Letters*, *43*(16), 8417–8425. https://doi.org/10.1002/2016GL070532

Brudy, M., & Zoback, M. D. (1999). Drilling-induced tensile wall-fractures: Implications for determination of in-situ stress orientation and magnitude. *International Journal of Rock Mechanics and Mining Sciences*, *36*(2), 191–215. https://doi.org/10.1016/S0148-9062(98)00182-X

Bunger, A. P., Detournay, E., & Garagash, D. I. (2005). Toughness-dominated hydraulic fracture with leak-off. *International Journal of Fracture*, *134*(2), 175–190. https://doi.org/10.1007/s10704-005-0154-0

Carslaw, H. S., & Jaeger, J. C. (1959). *Conduction of heat in solids* (2nd ed.). Clarendon Press.

Cha, M., Alqahtani, N. B., Yao, B., Yin, X., Kneafsey, T. J., Wang, L., et al. (2018). Cryogenic fracturing of wellbores under true triaxial-confining stresses: Experimental investigation. *SPE Journal*, *23*(04), 1271–1289. https://doi.org/10.2118/180071-pa

Cha, M., Alqahtani, N. B., Yin, X., Kneafsey, T. J., Yao, B., & Wu, Y.-S. (2017). Laboratory system for studying cryogenic thermal rock fracturing for well stimulation. *Journal of Petroleum Science and Engineering*, *156*, 780–789. https://doi.org/10.1016/j.petrol.2017.06.062

Cha, M., Yin, X., Kneafsey, T., Johanson, B., Alqahtani, N., Miskimins, J., et al. (2014). Cryogenic fracturing for reservoir stimulation – Laboratory studies. *Journal of Petroleum Science and Engineering*, *124*, 436–450. https://doi.org/10.1016/j.petrol.2014.09.003

Chaki, S., Takarli, M., & Agbodjan, W. P. (2008). Influence of thermal damage on physical properties of a granite rock: Porosity, permeability and ultrasonic wave evolutions. *Construction and Building Materials*, *22*(7), 1456–1461. https://doi.org/10.1016/j.conbuildmat.2007.04.002

Cheng, A. (2016). *Poroelasticity*. Springer International Publishing. https://doi.org/10.1007/978-3-319-25202-5

Chen, B., Barboza, B. R., Sun, Y., Bai, J., Thomas, H. R., Dutko, M., et al. (2021). A review of hydraulic fracturing simulation. *Archives of Computational Methods in Engineering*. https://doi.org/10.1007/s11831-021-09653-z

Chen, B., Barron, A. R., Owen, D. R. J., & Li, C.-F. (2018). Propagation of a plane strain hydraulic fracture with a fluid lag in permeable rock. *Journal of Applied Mechanics*, *85*(9). https://doi.org/10.1115/1.4040331

Chen, B., Cen, S., Barron, A. R., Owen, D. R. J., & Li, C. (2018). Numerical investigation of the fluid lag during hydraulic fracturing. *Engineering Computations*, *35*(5), 2050–2077. https://doi.org/10.1108/ec-02-2018-0087

Chen, B., Sun, Y., Barboza, B. R., Barron, A. R., & Li, C. (2020). Phase-field simulation of hydraulic fracturing with a revised fluid model and hybrid solver. *Engineering Fracture Mechanics*, *229*, 106928. https://doi.org/10.1016/j.engfracmech.2020.106928

Chen, B., & Zhou, Q. (2021). Propagation, arrest, and reactivation of thermally driven fractures in an unconfined half-space using stability analysis. *Theoretical and Applied Fracture Mechanics*, *114*, 102969. https://doi.org/10.1016/j.tafmec.2021.102969

Chu, D., Li, X., & Liu, Z. (2017). Study the dynamic crack path in brittle material under thermal shock loading by phase field modeling. *International Journal of Fracture*, *208*(1–2), 115–130. https://doi.org/10.1007/s10704-017-0220-4

Cihan, A., Zhou, Q., & Birkholzer, J. T. (2011). Analytical solutions for pressure perturbation and fluid leakage through aquitards and wells in multilayered-aquifer systems. *Water Resources Research*, *47*(10). https://doi.org/10.1029/2011wr010721

Crouch, S. L., & Starfield, A. M. (1983). *Boundary element methods in solid mechanics: With applications in rock mechanics and geological engineering*. George Allen & Unwin.

Daoud, A., Browning, J., Meredith, P. G., & Mitchell, T. M. (2020). Microstructural controls on thermal crack damage and the presence of a temperature-memory effect during cyclic thermal stressing of rocks. *Geophysical Research Letters*, *47*(19). https://doi.org/10.1029/2020gl088693

Demuth, R. B., & Harlow, F. H. (1980). *Geothermal energy enhancement by thermal fracture. [REX (Rock Energy Extraction)]*. Los Alamos Scientific Lab. https://doi.org/10.2172/6731510

Detienne, J. L., Creusot, M., Kessler, N., Sahuquet, B., & Bergerot, J. L. (1998). Thermally induced fractures: A field-proven analytical model. *SPE Reservoir Evaluation and Engineering*, *1*(1), 30–35. https://doi.org/10.2118/30777-PA

Detournay, E., & Cheng, A. H. D. (1988). Poroelastic response of a borehole in a non-hydrostatic stress field. *International Journal of Rock Mechanics and Mining Sciences & Geomechanics Abstracts*, *25*(3), 171–182. https://doi.org/10.1016/0148-9062(88)92299-1

Detournay, E., & Cheng, A. H. D. (1993). Fundamentals of poroelasticity. In C. Fairhurst (Ed.), *Analysis and design methods* (pp. 113–171). Pergamon. https://doi.org/10.1016/B978-0-08-040615-2.50011-3

EGI. (2019). *Frontier observatory for research in geothermal energy – Milford site, Utah, phase 2c section b: Results II. Dynamic reservoir modeling*. Energy and Geoscience Institute, University of Utah.

Enayatpour, S., & Patzek, T. (2013).Thermal shock in reservoir rock enhances the hydraulic fracturing of gas shales. Paper presented at the SPE/AAPG/SEG Unconventional Resources Technology Conference. https://doi.org/10.1190/urtec2013-153

Enayatpour, S., van Oort, E., & Patzek, T. (2019). Thermal cooling to improve hydraulic fracturing efficiency and hydrocarbon production in shales. *Journal of Natural Gas Science and Engineering*, *62*, 184–201. https://doi.org/10.1016/j.jngse.2018.12.008

Evans, K. F. (2005). Permeability creation and damage due to massive fluid injections into granite at 3.5 km at Soultz: 2. Critical stress and fracture strength. *Journal of Geophysical Research: Solid Earth*, *110*(B4). https://doi.org/10.1029/2004JB003169

Evans, K. F., Genter, A., & Sausse, J. (2005). Permeability creation and damage due to massive fluid injections into granite at 3.5 km at Soultz: 1. Borehole observations. *Journal of Geophysical Research: Solid Earth*, *110*(B4). https://doi.org/10.1029/2004JB003168

Fredrich, J. T., & Wong, T.-F. (1986). Micromechanics of thermally induced cracking in three crustal rocks. *Journal of Geophysical Research: Solid Earth*, *91*(B12), 12743–12764. https://doi.org/10.1029/JB091iB12p12743

Gao, Q., & Ghassemi, A. (2020). Three-dimensional thermo-poroelastic modeling and analysis of flow, heat transport and deformation in fractured rock with applications to a lab-scale geothermal system. *Rock Mechanics and Rock Engineering*, *53*(4), 1565–1586. https://doi.org/10.1007/s00603-019-01989-0

Geyer, J. F., & Nemat-Nasser, S. (1982). Experimental investigation of thermally induced interacting cracks in brittle solids. *International Journal of Solids and Structures*, *18*(4), 349–356. https://doi.org/10.1016/0020-7683(82)90059-2

Goodarzi, S., Settari, A., & Keith, D. (2012). Geomechanical modeling for CO_2 storage in Nisku aquifer in Wabamun Lake area in Canada. *International Journal of Greenhouse Gas Control*, *10*, 113–122. https://doi.org/10.1016/j.ijggc.2012.05.020

Gringarten, A. C. (1984). Interpretation of tests in fissured and multilayered reservoirs with double-porosity behavior: Theory and practice. *Journal of Petroleum Technology*, *36*(4), 549–564. https://doi.org/10.2118/10044-PA

Gudmundsson, A. (2011). Evolution of extension fractures. In *Rock fractures in geological processes* (pp. 373–415). Cambridge University Press. https://doi.org/10.1017/CBO9780511975684.014

Hantush, M. S. (1960). Modification of the theory of leaky aquifers. *Journal of Geophysical Research*, *65*(11), 3713–3725. https://doi.org/10.1029/JZ065i011p03713

Harlow, F. H., & Pracht, W. E. (1972). A theoretical study of geothermal energy extraction. *Journal of Geophysical Research*, *77*(35), 7038–7048. https://doi.org/10.1029/JB077i035p07038

Hasselman, D. P. H. (1963). Elastic energy at fracture and surface energy as design criteria for thermal shock. *Journal of the American Ceramic Society*, *46*(11), 535–540. https://doi.org/10.1111/j.1151-2916.1963.tb14605.x

Hofmann, M., Bahr, H. A., Weiss, H. J., Bahr, U., & Balke, H. (2011). Spacing of crack patterns driven by steady-state cooling or drying and influenced by a solidification boundary. *Physical Review E*, *83*(3), 036104. https://doi.org/10.1103/PhysRevE.83.036104

Huang, H., Meakin, P., & Malthe-Sorenssen, A. (2016). Physics-based simulation of multiple interacting crack growth in brittle rocks driven by thermal cooling. *International Journal for Numerical and Analytical Methods in Geomechanics*, *40*(16), 2163–2177. https://doi.org/10.1002/nag.2523

Hubbert, M. K., & Willis, D. G. (1957). Mechanics of hydraulic fracturing. *Transactions of the AIME*, *210*(1), 153–168. https://doi.org/10.2118/686-g

Jaeger, J. C., Cook, N. G. W., & Zimmerman, R. W. (2007). *Fundamentals of rock mechanics*. Wiley-Blackwell.

Jenkins, D. R. (2005). Optimal spacing and penetration of cracks in a shrinking slab. *Physical Review E*, *71*(5 Pt 2), 056117. https://doi.org/10.1103/PhysRevE.71.056117

Jiang, C. P., Wu, X. F., Li, J., Song, F., Shao, Y. F., Xu, X. H., et al. (2012). A study of the mechanism of formation and numerical simulations of crack patterns in ceramics subjected to thermal shock. *Acta Materialia*, *60*(11), 4540–4550. https://doi.org/10.1016/j.actamat.2012.05.020

Kitao, K., Ariki, K., Watanabe, H., & Wakita, K. (1995). Cold-water well stimulation experiments in the Sumikawa Geothermal field, Japan. *Geothermal Resources Council - Bulletin*, *24*, 53–61.

Koning, E. J. L. (1985). *Fractured water injection wells – Analytical modelling of fracture propagation*. (pp. 57). Society of Petroleum Engineers.

Koning, E. J. L., & Niko, H. (1985). Fractured water-injection wells: A pressure falloff test for determining fracture dimensions. Paper presented at the SPE Annual Technical Conference and Exhibition. https://doi.org/10.2118/14458-ms

Lecampion, B., & Detournay, E. (2007). An implicit algorithm for the propagation of a hydraulic fracture with a fluid lag. *Computer Methods in Applied Mechanics and Engineering*, *196*(49–52), 4863–4880. https://doi.org/10.1016/j.cma.2007.06.011

Liu, F., Fu, P., Mellors, R. J., Plummer, M. A., Ali, S. T., Reinisch, E. C., et al. (2018). Inferring geothermal reservoir processes at the Raft River geothermal field, Idaho, USA, through modeling InSAR-measured surface deformation. *Journal of Geophysical Research: Solid Earth*, *123*(5), 3645–3666. https://doi.org/10.1029/2017jb015223

Li, N., Zhang, S., Wang, H., Ma, X., Zou, Y., & Zhou, T. (2021). Effect of thermal shock on laboratory hydraulic fracturing in Laizhou granite: An experimental study. *Engineering Fracture Mechanics*, *248*, 107741. https://doi.org/10.1016/j.engfracmech.2021.107741

Loret, B. (2019). Enhanced geothermal systems (EGS): Hydraulic fracturing in a thermo-poroelastic framework. In *Fluid injection in deformable geological formations: Energy related issues* (pp. 465–551). Springer International Publishing. https://doi.org/10.1007/978-3-319-94217-9_7

Lu, G., Gordeliy, E., Prioul, R., Aidagulov, G., Uwaifo, E. C., Ou, Q., et al. (2020). Time-dependent hydraulic fracture initiation. *Journal of Geophysical Research: Solid Earth*, *125*(3). https://doi.org/10.1029/2019jb018797

Lu, G., Gordeliy, E., Prioul, R., & Bunger, A. (2017). Modeling initiation and propagation of a hydraulic fracture under subcritical conditions. *Computer Methods in Applied Mechanics and Engineering*, *318*, 61–91. https://doi.org/10.1016/j.cma.2017.01.018

Martínez-Garzón, P., Kwiatek, G., Sone, H., Bohnhoff, M., Dresen, G., & Hartline, C. (2014). Spatiotemporal changes, faulting regimes, and source parameters of induced seismicity: A case study from the Geysers geothermal field. *Journal of Geophysical Research: Solid Earth*, *119*(11), 8378–8396. https://doi.org/10.1002/2014jb011385

Martins, J. P., Murray, L. R., Clifford, P. J., McLelland, W. G., Hanna, M. F., & Sharp, J. W., Jr. (1995). Produced-water reinjection and fracturing in Prudhoe bay. *SPE Reservoir Engineering*, *10*(03), 176–182. https://doi.org/10.2118/28936-PA

McTigue, D. F. (1986). Thermoelastic response of fluid-saturated porous rock. *Journal of Geophysical Research: Solid Earth*, *91*(B9), 9533–9542. https://doi.org/10.1029/JB091iB09p09533

Menouillard, T., & Belytschko, T. (2010). Dynamic fracture with meshfree enriched XFEM. *Acta Mechanica*, *213*(1–2), 53–69. https://doi.org/10.1007/s00707-009-0275-z

Mériaux, C., & Lister, J. R. (2002). Calculation of dike trajectories from volcanic centers. *Journal of Geophysical Research: Solid Earth*, *107*(B4), ETG 10-1–ETG 10-10. https://doi.org/10.1029/2001jb000436

Miehe, C., Schänzel, L.-M., & Ulmer, H. (2015). Phase field modeling of fracture in multi-physics problems. Part I. Balance of crack surface and failure criteria for brittle crack propagation in thermo-elastic solids. *Computer Methods in Applied Mechanics and Engineering*, *294*, 449–485. https://doi.org/10.1016/j.cma.2014.11.016

Morales, R. H., Abou-Sayed, A. S., Jones, A. H., & Al-Saffar, A. (1986). Detection of a formation fracture in a waterflooding experiment. *Journal of Petroleum Technology*, *38*(10), 1113–1121. https://doi.org/10.2118/13747-PA

Murphy, H. D. (1978). *Thermal stress cracking and the enhancement of heat extraction from fractured geothermal reservoirs*. Los Alamos Scientific Lab. https://doi.org/10.2172/6771724

Nemat-Nasser, S., Keer, L. M., & Parihar, K. S. (1978). Unstable growth of thermally induced interacting cracks in brittle solids. *International Journal of Solids and Structures*, *14*(6), 409–430. https://doi.org/10.1016/0020-7683(78)90007-0

Nemat-Nasser, S., & Oranratnachai, A. (1979). Minimum spacing of thermally induced cracks in brittle solids. *Journal of Energy Resources Technology*, *3*, 34–40. https://doi.org/10.1115/1.3446859

Nemat-Nasser, S., Sumi, Y., & Keer, L. M. (1980). Unstable growth of tension cracks in brittle solids: Stable and unstable bifurcations, snap-through, and imperfection sensitivity. *International Journal of Solids and Structures*, *16*(11), 1017–1035. https://doi.org/10.1016/0020-7683(80)90102-X

Patterson, J. W., & Driesner, T. (2021). Elastic and thermoelastic effects on thermal water convection in fracture zones. *Journal of Geophysical Research: Solid Earth*, *126*(2). https://doi.org/10.1029/2020jb020940

Pearson, C. F., Fehler, M. C., & Albright, J. N. (1983). Changes in compressional and shear wave velocities and dynamic moduli during operation of a hot dry rock geothermal system. *Journal of Geophysical Research: Solid Earth*, *88*(B4), 3468–3475. https://doi.org/10.1029/JB088iB04p03468

Perkins, T. K., & Gonzalez, J. A. (1984). Changes in earth stresses around a wellbore caused by radially symmetrical pressure and temperature gradients. *Society of Petroleum Engineers Journal*, *24*(2), 129–140. https://doi.org/10.2118/10080-PA

Perkins, T. K., & Gonzalez, J. A. (1985). The effect of thermoelastic stresses on injection well fracturing. *Society of Petroleum Engineers Journal*, *25*(1), 78–88. https://doi.org/10.2118/11332-PA

Rangriz Shokri, A., Chalaturnyk, R. J., & Nickel, E. (2019). Non-isothermal injectivity considerations for effective geological storage of CO2 at the Aquistore site, Saskatchewan, Canada. Paper presented at the SPE Annual Technical Conference and Exhibition. https://doi.org/10.2118/196118-MS

Raterman, K. T., Farrell, H. E., Mora, O. S., Janssen, A. L., Gomez, G. A., Busetti, S., et al. (2018). Sampling a stimulated rock volume: An eagle ford example. *SPE Reservoir Evaluation and Engineering*, *21*(4), 927–941. https://doi.org/10.2118/191375-PA

Raterman, K. T., Liu, Y., & Warren, L. (2019). Analysis of a drained rock volume: An eagle ford example. Paper presented at the 7th Unconventional Resources Technology Conference.

Rice, J. D. (1968). Mathematical analysis in the mechanics of fracture. In H.Liebowitz (Ed.), *Fracture: An advanced treatise* (Vol. 2, pp. 191–311). Academic Press.

Robertson, E. C. (1988). *Thermal properties of rocks*. U.S. Geology Survey. https://doi.org/10.3133/ofr88441

Rummel, F., & Hansen, J. (1989). Interpretation of hydrofrac pressure recordings using a simple fracture mechanics simulation model. *International Journal of Rock Mechanics and Mining Sciences & Geomechanics Abstracts*, *26*(6), 483–488. https://doi.org/10.1016/0148-9062(89)91425-3

Salimzadeh, S., Nick, H. M., & Zimmerman, R. W. (2018). Thermoporoelastic effects during heat extraction from low-permeability reservoirs. *Energy*, *142*, 546–558. https://doi.org/10.1016/j.energy.2017.10.059

Salimzadeh, S., Paluszny, A., & Zimmerman, R. W. (2016). Thermal effects during hydraulic fracturing in low-permeability brittle rocks. *Paper presented at the 50th on U.S. Rock Mechanics/Geomechanics Symposium*.

Salimzadeh, S., Paluszny, A., & Zimmerman, R. W. (2017). Three-dimensional poroelastic effects during hydraulic fracturing in permeable rocks. *International Journal of Solids and Structures*, *108*, 153–163. https://doi.org/10.1016/j.ijsolstr.2016.12.008

Salimzadeh, S., Paluszny, A., & Zimmerman, R. W. (2018). Effect of cold CO_2 injection on fracture apertures and growth. *International Journal of Greenhouse Gas Control*, *74*, 130–141. https://doi.org/10.1016/j.ijggc.2018.04.013

Schmitt, D. R., & Zoback, M. D. (1989a). Laboratory tests of the effects of pore pressure on tensile failure. *Paper presented at the ISRM International Symposium*.

Schmitt, D. R., & Zoback, M. D. (1989b). Poroelastic effects in the determination of the maximum horizontal principal stress in hydraulic fracturing tests—A proposed breakdown equation employing a modified effective stress relation for tensile failure. *International Journal of Rock Mechanics and Mining Sciences & Geomechanics Abstracts*, *26*(6), 499–506. https://doi.org/10.1016/0148-9062(89)91427-7

Shao, Y., Zhang, Y., Xu, X., Zhou, Z., Li, W., Liu, B., & Jin, Z. H. (2011). Effect of crack pattern on the residual strength of ceramics after quenching. *Journal of the American Ceramic Society*, *94*(9), 2804–2807. https://doi.org/10.1111/j.1551-2916.2011.04728.x

Shen, Y.-J., Hao, J.-S., Hou, X., Yuan, J.-Q., & Bai, Z.-P. (2021). Crack propagation in high-temperature granite after cooling shock: Experiment and numerical simulation. *Bulletin of Engineering Geology and the Environment*, *80*, 5831–5844. https://doi.org/10.1007/s10064-021-02259-6

Siratovich, P., Sass, I., Homuth, S., & Bjornsson, A. (2011). Thermal stimulation of geothermal reservoirs and laboratory investigation of thermally induced fractures. *Transactions – Geothermal Resources Council*, *35*, 1529–1535.

Stefansson, I., Keilegavlen, E., Halldórsdóttir, S., & Berre, I. (2021). Numerical modelling of convection-driven cooling, deformation and fracturing of thermo-poroelastic media. *Transport in Porous Media*, *140*(1), 371–394. https://doi.org/10.1007/s11242-021-01676-1

Stephens, G., & Voight, B. (1982). Hydraulic fracturing theory for conditions of thermal stress. *International Journal of Rock Mechanics and Mining Sciences & Geomechanics Abstracts*, *19*(6), 279–284. https://doi.org/10.1016/0148-9062(82)91364-X

Svendson, A. P., Wright, M. S., Clifford, P. J., & Berry, P. J. (1991). Thermally induced fracturing of Ula water injectors. *SPE Production Engineering*, *6*(4), 384–390. https://doi.org/10.2118/20898-PA

Tang, S. B., Wang, J., & Chen, P. (2020). Theoretical and numerical studies of cryogenic fracturing induced by thermal shock for reservoir stimulation. *International Journal of Rock Mechanics and Mining Sciences*, *125*, 104160. https://doi.org/10.1016/j.ijrmms.2019.104160

Tang, S. B., Zhang, H., Tang, C. A., & Liu, H. Y. (2016). Numerical model for the cracking behavior of heterogeneous brittle solids subjected to thermal shock. *International Journal of Solids and Structures*, *80*, 520–531. https://doi.org/10.1016/j.ijsolstr.2015.10.012

Tarasovs, S., & Ghassemi, A. (2011). Propagation of a system of cracks under thermal stress. *Paper presented at the 45th U.S. Rock Mechanics/Geomechanics Symposium*.

Tarasovs, S., & Ghassemi, A. (2014). Self-similarity and scaling of thermal shock fractures. *Physical Review E*, *90*(1), 012403. https://doi.org/10.1103/PhysRevE.90.012403

Terzaghi, K. (1936). The shearing resistance of saturated soils and the angle between the planes of shear. *Paper presented at the First International Conference on Soil Mechanics*. Harvard University

van den Hoek, P. J., Matsuura, T., de Kroon, M., & Gheissary, G. (1999). Simulation of produced water reinjection under fracturing conditions. *SPE Production and Facilities*, *14*(3), 166–176. https://doi.org/10.2118/57385-PA

Vidal, J., Genter, A., & Schmittbuhl, J. (2016). Pre- and post-stimulation characterization of geothermal well GRT-1, Rittershoffen, France: Insights from acoustic image logs of hard fractured rock. *Geophysical Journal International*, *206*(2), 845–860. https://doi.org/10.1093/gji/ggw181

Vilarrasa, V., Olivella, S., Carrera, J., & Rutqvist, J. (2014). Long term impacts of cold CO_2 injection on the caprock integrity. *International Journal of Greenhouse Gas Control*, *24*, 1–13. https://doi.org/10.1016/j.ijggc.2014.02.016

Wang, B., Li, J. E., & Yang, C. (2015). Thermal shock fracture mechanics analysis of a semi-infinite medium based on the dual-phase-lag heat conduction model. *Proceedings of the Royal Society A: Mathematical, Physical and Engineering*, *471*(2174), 20140595. https://doi.org/10.1098/rspa.2014.0595

Wang, F., & Konietzky, H. (2019). Thermo-mechanical properties of granite at elevated temperatures and numerical simulation of thermal cracking. *Rock Mechanics and Rock Engineering*, *52*(10), 3737–3755. https://doi.org/10.1007/s00603-019-01837-1

Wang, F., Konietzky, H., Frühwirt, T., Li, Y., & Dai, Y. (2019). The influence of temperature and high-speed heating on tensile strength of granite and the application of digital image correlation on tensile failure processes. *Rock Mechanics and Rock Engineering*, *53*(4), 1935–1952. https://doi.org/10.1007/s00603-019-02022-0

Wang, H. F., Bonner, B. P., Carlson, S. R., Kowallis, B. J., & Heard, H. C. (1989). Thermal stress cracking in granite. *Journal of Geophysical Research: Solid Earth*, *94*(B2), 1745–1758. https://doi.org/10.1029/JB094iB02p01745

Williams, D. B., Sherrard, D. W., & Lin, C. Y. (1987). The impacts on waterflood management of inducing fractures in injection wells in the Prudhoe Bay Oil Field. *Paper presented at the SPE California Regional Meeting*. https://doi.org/10.2118/16358-MS

Wu, X., Huang, Z., Zhang, S., Cheng, Z., Li, R., Song, H., et al. (2019). Damage analysis of high-temperature rocks subjected to LN2 thermal shock. *Rock Mechanics and Rock Engineering*, *52*(8), 2585–2603. https://doi.org/10.1007/s00603-018-1711-y

Zhang, S., Huang, Z., Zhang, H., Guo, Z., Wu, X., Wang, T., et al. (2018). Experimental study of thermal-crack characteristics on hot dry rock impacted by liquid nitrogen jet. *Geothermics*, *76*, 253–260. https://doi.org/10.1016/j.geothermics.2018.08.002

Zhang, X., Jeffrey, R. G., & Thiercelin, M. (2009). Mechanics of fluid-driven fracture growth in naturally fractured reservoirs with simple network geometries. *Journal of Geophysical Research*, *114*(B12). https://doi.org/10.1029/2009jb006548

Zhang, Z., Li, X., He, J., Wu, Y., & Zhang, B. (2015). Numerical analysis on the stability of hydraulic fracture propagation. *Energies*, *8*(9), 9860–9877. https://doi.org/10.3390/en8099860

Zhou, Q., Oldenburg, C. M., & Rutqvist, J. (2019). Revisiting the analytical solutions of heat transport in fractured reservoirs using a generalized multirate memory function. *Water Resources Research*, *55*(2), 1405–1428. https://doi.org/10.1029/2018wr024150

Zhou, Q., Oldenburg, C. M., Rutqvist, J., & Birkholzer, J. T. (2017). Revisiting the fundamental analytical solutions of heat and mass transfer: The kernel of multirate and multidimensional diffusion. *Water Resources Research*, *53*(11), 9960–9979. https://doi.org/10.1002/2017WR021040

Zhou, Q., Oldenburg, C. M., Spangler, L. H., & Birkholzer, J. T. (2017). Approximate solutions for diffusive fracture-matrix transfer: Application to storage of dissolved CO_2 in fractured rocks. *Water Resources Research*, *53*(2), 1746–1762. https://doi.org/10.1002/2016wr019868

Zhou, Q., Yang, X., Zhang, R., Hosseini, S. A., Ajo-Franklin, J. B., Freifeld, B. M., et al. (2020). Dynamic processes of CO_2 storage in the field: 1. Multiscale and multipath channeling of CO_2 flow in the hierarchical fluvial reservoir at Cranfield, Mississippi .*Water Resources Research*, *56*(2), e2019EF001360. https://doi.org/10.1029/2019WR025688

Zoback, M. (2007). *Reservoir geomechanics*. Cambridge University Press. https://doi.org/10.1017/CBO9780511586477